Title
A DRIFT CHAMBER FOR HIGH-ENERGY HEAVY-IONS

Author
Kobayashi, T.

Publication Date
1986-09-01

LBL-22164
Preprint

Lawrence Berkeley Laboratory
UNIVERSITY OF CALIFORNIA

Submitted to Nuclear Instruments and Methods

A DRIFT CHAMBER FOR HIGH-ENERGY HEAVY-IONS

T. Kobayashi, F.S. Bieser, T.J.M. Symons,
and D.E. Greiner

September 1986

NUCLEAR SCIENCE DIVISION

Prepared for the U.S. Department of Energy under Contract DE-AC03-76SF00098

A Drift Chamber for High-Energy Heavy-Ions

Toshio Kobayashi [*], *F. S. Bieser, T. J. M. Symons, and D. E. Greiner*
Lawrence Berkeley Laboratory, University of California, Berkeley, CA 94720

ABSTRACT

We have constructed and tested a prototype drift chamber for tracking heavy projectile fragments produced in nucleus-nucleus collisions in the GeV/nucleon energy range. By adjusting the gas gain, position resolution of less than 200 microns can be achieved for several overlapping ranges of particle charge with virtually 100% efficiency. The chamber was successfully operated for tracking various projectile fragments produced from an ^{40}Ar beam at 1.65 GeV/nucleon with a single high voltage setting.

1. Introduction

From high-energy nucleus-nucleus reactions in the GeV/nucleon energy range, heavy projectile fragments are produced within a narrow cone (≤ 2 degrees) centered at zero degrees [1]. This kinematic focusing effect is one of the merits in heavy-ion collisions, since a rather small detector is enough to study phenomena in the projectile frame. In such cases, particle identification (charge Z, mass A and momentum vector P) is necessary for multi particles in the event. Since no single experimentally measured quantity can provide both mass and momentum, two independent measurements in addition to the charge measurement are necessary for full particle identification. In the Heavy Ion Spectrometer System (HISS) under development at the LBL Bevalac [2], drift chambers are used to measure the magnetic deflection of each particle and hence its rigidity R (= total momentum / charge), and direct time of flight or pulse height of Cerenkov counters operated right at the total internal reflection threshold to measure the velocity [3]. Cerenkov counters operated far from the total internal reflection threshold [3] or multiple sampling ionization chambers [4] are also used to measure the charge. The mass resolution depends on the rigidity and velocity(β) resolution as follows:

$$\left(\frac{\delta A}{A}\right)^2=\left(\frac{\delta R}{R}\right)^2+\left(\frac{\delta Z}{Z}\right)^2+\left(\gamma^2\frac{\delta\beta}{\beta}\right)^2$$

In order to separate isotopes around mass 100, rigidity resolution of 2×10^{-3} is suitable for light particles (Fig. 2-2a) and for heavy particles (Fig. 2-2b). The magnitude of the electric field in the median plane of the drift cell is shown in Fig. 2-3. The minimum electric field in both cases is larger than 0.4 KV/cm, which is well beyond the drift velocity saturation voltage of the P10 gas (90% Ar, 10% CH4) used in the test.

The wire cathode allows interference between consecutive planes of field-shaping structures so that some considerable space is required between them. A guard plane (75 micron Cu-Be wires in 8mm pitch) operated at ground potential decouples the electric field and collects the ionizing electrons produced by the track outside the sensitive volume of the cell. This increases the pulse height uniformity across the cell and also prevents the slow ionizations to drift from the inactive region into the cell for the constant fraction discriminators. However this guard plane can not be too close to either cathode plane or it will reduce the gain on the anodes. The effect of guard planes is also included in Fig. 2-2.

2.2. Plane Arrangement and Construction

A complete prototype drift chamber consists of 12 modular planes with three kinds of wire orientation (S: 0 deg ,T: +60 deg , U: -60 deg) as shown schematically in Fig. 2-4. These modules are arranged as S-T-U-S'-T'-U'-S'-T'-U'-S-T-U, where S', T' and U' have anodes offset by one half a cell width to solve the left-right ambiguity. The sense planes are distributed along the beam axis 10 cm apart with guard planes in between, such that 12 planes give a 1.1 meter lever arm for good momentum reconstruction. This uniform distribution helps the track finding algorithm as mentioned in the introduction. The total sensitive area of the prototype is 40cm(Hor.) x 30cm(Vert.) x 120cm(Long) with 352 sense wires.

The cross section of one module is shown in Fig. 2-5. All anode and field-shaping wires were mounted on 4mm thick NEMA G-10 frames. Sets of two cathode planes, one sense plane, one guard plane, and three 1mm thick rubber gaskets were bolted to a stiffener frame made from 3/4 inch thick aluminum tooling plate. This frame also provided reference edges for precise location of each module. The exact location of all wires relative to these reference edges was measured using an optical interferometer system with an accuracy of 10 microns. All wire positions were fitted by a simple formula and the deviation of measured points from the formula had a standard deviation of 40 microns.

After the 12 modular planes were assembled and measured, they were mounted on a rigid aluminum base plate with an accurate separation between them using long bars with notches. This procedure provided good mechanical rigidity and precise relative positioning. Silicone rubber sealant and aluminum strips closed the spaces between the modules and 50 micron Mylar windows closed the gas volume at the front and rear. The completed prototype chamber is shown in Fig. 2-6.

3. Electronics and readouts

3.1. Choice of Constant Fraction discrimination (CFD)

The most important requirement on the time pickup circuit of the drift chamber in this particular application is its capability to pickup the timing signal from the heavy core ionization among many background δ-rays which might distort the timing signal of core ionization. A constant fraction discriminator (CFD) which will be described in the next section was chosen as the best compromise for dealing with the wide dynamic range of the signals produced by the high-energy heavy ions. For particles with $Z=1$ and 2, a simple leading edge discriminator would work well as most frontends are designed for. For high Z particles which produce rather uniform sheaths of δ-rays, a centroid finder would probably give the best results. Our fraction (80%) comes close to the ideal case. As we can see in section 5-1, it is impossible to use the leading edge discriminator if wide dynamic range in particle charges is required, since the timing from the leading edge would reflect the δ-ray cloud better than the primary track. Particles with $Z=6$ at 1.3 GeV/A produce approximately one energetic δ-ray (whose range is longer than 5mm) per path length in the chamber. If this δ-ray is on the side of the track nearest the anode, a leading edge discriminator would trigger on it and not on the heavy ion. Our design of CFD avoids this kind of mistake, i.e. the circuit will pick up only the largest pulse during the maximum drift time of $\approx$250 nsec. A schematic diagram of the circuit is shown in Fig. 3-1 with pulse shapes at several points in the circuit expected from light ions such as carbon.

3.2. Front-End design

The complete front-end circuit is shown in Fig. 3-2. A common base input stage converts the current signals to voltage pulses with an effective transimpedance of 2 K ohms. After a 500 nsec delay line, this linear signal is sent over 50 ohm ribbon coax to the current integrating ADC's. A nonlinear amplifier precedes the discriminator to compress the range of signals presented to the comparator (AM 685). The minimum usable threshold for the AM685 is 10mV, while the maximum permissible input voltage is 4 volts, making a dynamic range of 400:1. For small signals it has a gain of -30 (with inversion) while for very large signals the gain is only -1. While this signal is travelling through a 250nsec delay line, a peak sensor stores the largest pulse height (with a decay time constant of 1000 nsec.). The delayed pulse and the slightly attenuated peak voltage are presented to a fast comparator making a constant fraction discriminator. The "fraction" is determined by the attenuation through the delay line and the decay time-constant of the peak sensor relative to the delay line length; in our case, approximately 80%. The inputs are biased to provide a minimum threshold of 1 microamp (effective input) to prevent oscillation. The comparator output is fed back to the latch-control to give a monostable width of 1 microsecond.

The CFD is , generally speaking, sensitive to the input pulse shape or rise time. In addition to this effect, we also observe a large time slew effect depending on the input pulse height. This turns out to be caused by variation in the non-linear amplifier's rise time. Fig. 3-3 shows the time slew effect (time shift) as a function of input pulse current while keeping the rise time constant (20 nsec), checked by a test pulse. The time slew effect is large. However, it can be corrected using pulse height information in the offline analysis.

3.3. Other electronics and data-acquisition system

The front-ends were mounted directly on the chamber. The threshold of the CFD was set at 2 μA during the run without any noise problems. The ECL level logic signals from the front-ends were sent to a Lecroy 4290 TDC system via 50 foot long twisted pair cables, and then timed with an accuracy of 1 nsec/ch. The preamplified analog signals were transferred to a Lecroy 2280 ADC system (charge integrating ADC) in the counting area via 150 foot long multi-coaxial cables. The ADC input was modified into a quasi-differential mode to reject the line noise. Attenuators were put at the input of the 2280 ADC modules in some part of the first test runs when Xe and U ions were studied. All the electronics were calibrated with test pulses into the frontends via capacitive coupling. This is used to check dead channels and to adjust the slope and offset of the TDC's.

One disadvantage of this system is that there are independent thresholds for the time and pulse height information: the discriminator threshold for the 4290 TDC system and the digital threshold for the 2280 ADC system after pedestal subtraction. The digital threshold of the ADC system was set at $\approx 3\sigma$ level of the noise level , but this level was much higher than the threshold of the discriminator. This caused some complications in the track finding efficiency in the offline analysis, since pulse height information turns out to be quite important to correct the time slew effect.

The TDCs and ADCs together with information from other detector systems were read into a large memory module (512K bytes) in a camac crate via an MBD11 (Micro-Programmed Branch Driver) during the beam-on period (0.5 sec), and then transferred to magnetic tape on a PDP 11/45 during the beam-off period (4 sec). This system had a capability to transfer raw data at up to 300 K bytes /spill. Due to a large number of spurious hits from δ-rays, we were sometimes forced to handle about 700 words/event in the xenon and uranium runs at some higher voltage settings.

4. Experimental Procedure

The drift chamber system was tested using heavy ion beams from the Bevalac at the Lawrence Berkeley Laboratory. In a first beam test run, primary and secondary beams were passed through the chamber. In a second run, projectile fragments from ^{40}Ar beam were detected using the prototype chamber.

4.1. Beam test run

In the first test run, variety of primary and secondary beams [6] from the Bevalac were used at an energy of ≈1 GeV/nucleon. Beam particles used were $^{3}_{1}$t, $^{6}_{2}$He, $^{9}_{3}$Li, $^{7}_{4}$Be, $^{10}_{5}$B, $^{20}_{10}$Ne, $^{56}_{26}$Fe, $^{132}_{54}$Xe, and $^{238}_{92}$U. The particle trajectory was defined by two sets of 1mm-spacing multiwire chambers (MWPC) placed upstream and downstream of the drift chamber. A scintillation counter was used to identify the charge of the particle, and it also gave a timing trigger signal. The high voltage of the MWPCs was adjusted to maximize the probability of a single hit (or cluster) for the heavy ion beams. Typically, the optimum high voltage of MWPCs for $_{54}$Xe beam was 1.3 KV less than that for protons at the same velocity. The digital threshold of 2280 ADC system was set at 15 channel.

During these runs, we studied the basic response of the chamber including pulse shape, single plane efficiency, pulse height distribution, and single plane position resolution as a function of particle charge and chamber high voltage.

4.2. Measurement of projectile fragments from ^{40}Ar

In the fragmentation measurement, we measured various projectile fragments ($4 \leq Z \leq 16$) from the fragmentation of $^{40}_{18}$Ar nucleus at 1.65 GeV/nucleon. This experiment was part of a systematic study of projectile fragments using heavy ion beams from ^{40}Ar to ^{137}La. The drift chamber was placed after the HISS spectrometer magnet (field integral is ≈5.5 tesla meter) to measure the rigidity of the fragments, together with other detectors for a full particle identification. The drift chamber was also sandwiched by 2 sets of 2mm-spacing MWPC to get an approximate estimate on the charge dependent time-to-distance relation. We used two different high voltage settings for defining MWPCs to cover the charge of the fragment for $4 \leq Z < 10$ and $10 \leq Z \leq 18$ separately. The high voltage of the drift chamber was set at - 1.3 KV, since we estimated from data of first test run that this voltage would cover from $Z = 5$ to $Z = 57$. The digital threshold of the 2280 ADC system was set at 25 channel due to higher noise level compared with the first test run.

In the analysis of this experiment, we have studied more detailed tests including the track-finding algorithm, the charge dependent time-to-distance relation, and the overall position resolution.

5. Results of the beam test run

In this chapter, we will discuss the basic response of the prototype drift chamber to various beams ranging from tritons to uranium at $\approx$ 1 GeV/nucleon.

5.1. Signal characteristics

The ultimate position resolution of our drift chamber may be limited by changes in the pulse shape presented to the CFD. In the following discussion, the chamber signals were photographed after the common base pre-amplifier on the front-end board. The traces have been redrawn to accentuate the crucial features.

6 KeV x-rays from ^{55}Fe source provide a baseline measurement for the preamplifier response since their ionization is localized to a single point in space. At the operating condition for low-Z particles (HV=-1.5KV), the signal has a 20nsec rise time and an exponential decay time of 100nsec. As expected, there is no position dependence on the pulse shape or amplitude. Linearity was checked by comparing the 5.9 KeV peak with the 3.0 KeV escape peak of Argon as shown in Fig. 5-1. At this voltage, the gas gain is approximately 7×10^4.

5 MeV alpha particles from ^{241}Am source deposit the same energy in a cell as a relativistic Sn ion but without δ-rays. We found the signal shape change for tracks near the anode: the peak amplitude is lower with a flattened top while the integrated charge remains unchanged. This is due to variations in the arrival time of ionizing electrons at the anode wire. The rise time, determined by the separation of positive ions from the first few avalanches, remains almost unchanged. Nevertheless, the CFD timing is effected since the decay of the peak sensor is held up by the flat top which raises the "fractional" threshold as the leading edge comes out of the 250nsec delay line.

In order to study the pulse shapes from heavy ions, the oscilloscope was triggered by a single wire in the upstream MWPC when beam particle passed approximately 5mm from the anode wire of the drift chamber. Fig. 5-3 shows the effect of increasing high voltage on signals from $_{54}$Xe and $_{92}$U ions. Notice that the rise time is comparable to the x-ray response at the lowest voltage. But the rise time increases until it is comparable to the total drift time as the gas gain is increased. Relativistic Xenon ions produce hundreds of δ-rays per centimeter along path length with approximately 60 δ-rays having a range greater than 5mm in Argon. This sea of ionization can not be resolved by the electronics but is integrated into a smooth long pulse. It is clear from these figures that a leading edge discriminator is not useful if we need a large dynamic range in particle charge. Lighter ions (Z $\approx$ 5) produce, on average, one energetic δ-ray in a drift cell which is distinguishable from the core ionization. It is for this regime that the CFD technique is essential. As we have discussed in section 3-1, we believe that our CFD is the best compromise to handle these two extreme cases .

5.2. Single plane efficiency

The single plane particle detection efficiency was studied for several different beams as a function of high voltage using data from the TDC. Efficiency plateau curves are shown in Fig. 5-4 for light ions from Z=1 to Z=5. The solid lines are for at least one hit per track per plane, while the dashed lines are for events with a single (one and only one) hit. As the energy loss increases with higher Z, the plateau voltage decreases by $\approx$50 volts per $\delta Z = 1$. When the chamber is operated at -1.5KV to have full efficiency for Z=1, the probability of a single hit for Z=5 is less than 50% due to δ-rays penetrating adjacent cells.

The efficiency for heavier beams ($Z \geq 10$) is essentially 100% above -1.0KV. The average number of hits per plane is shown in Fig. 5-5 as a function of incident charge and operating voltage. It should be noted that there are only twenty sense wires in a plane covering 20 cm on each side of the beam track. It is clear from the figure that there is no single operating voltage which can cover a wide range of particles with single hit response. We need to handle a large number of spurious hits from δ-rays whenever a large dynamic range of particle charge is required.

For applications with limited dynamic range, a lower operating voltage can be used, however even this approach has some limitations. In the region around Z$\approx$5, δ-rays can deposit as much energy in a cell as the primary track. There is no voltage that will guarantee a single hit response in this regime. With increased Z, the number of δ-rays increases but their energy spectrum remains unchanged. As the core ionization increases with Z^2, it becomes possible again to separate it from the surrounding sea of δ-rays if there is no saturation in the gas amplification. The optimum operating voltages for single hit response are estimated to be -0.5KV, -0.65KV and -0.85KV for Uranium, Xenon and Iron, respectively. Even here, there is a problem: our cell structure necessitated by high segmentation is such that the drift field is coupled to the gas gain unlike drift chambers with a much larger length to thickness ratio [7]. If we keep the drift gradient high enough to maintain a saturated drift velocity while lowering the gas gain, some electric field lines will terminate on field-shaping wires instead of focusing all the drifting electrons onto the anode wire. The situation is much worse for the Walenta-type drift chamber which will be described briefly in the appendix.

5.3. Pulse Height Information

5.3.1. Separation between primary track and δ-rays

While the chamber can have full detection efficiency over a wide dynamic range of particle charges, it is still necessary to eliminate spurious hits due to δ-rays. As an example, raw wire patterns of the drift chamber and MWPC's are shown in Fig. 5-6(1) at -1.2KV for iron(a), xenon(b), and uranium(c). Testing on the triangle condition among three orientations (S, T, and U) to find the track becomes , generally speaking, unfeasible due to the multitude of possible combinations, e.g. 8000 combinations to be checked for one triplet for Uranium. Besides taking too long, this would yield many accidental tracks. Additional pulse height information from the wire turns out to be very useful in finding the cell hit by the heavy ion as far as the heaviest particle in the event is concerned.

First, we studied the pulse height in the cell as a function of the distance from the primary track. Fig. 5-7 shows the pulse height spectra as a function of cell number. The MWPC information is used to determine the cell hit by the primary beam. From the figures, it is clear that the pulse height due to the primary track stands out as the largest pulse in a single plane. Thus it is possible to locate the cell containing the primary track by selecting the cell with the largest pulse height in the plane. Wire patterns from the same event after the pulse height selection are also shown in Fig. 5-6(2).

5.3.2. Pulse height distribution of heavy ions ($26 \leq Z \leq 92$)

The pulse height distributions from $_{26}$Fe tracks in a single plane are shown in Fig. 5-8(a). All wires with signals above threshold are included in the histgram. High voltages are changed from -1.1KV to -1.5KV in 0.1KV step. A clean separation between the core ionization and δ-rays can be seen at lower voltages. The pulse height separation between the primary track and δ-rays is, in principle, large for ions heavier than Iron as far as the chamber is operated in a semi proportional region. As the voltage becomes higher, the δ-ray spectrum merges into the core ionization distribution until they are completely overlapped. This worse S/N ratio seems to be caused by the saturation of pulses from the primary track.

Fig. 5-8 (b) shows the pulse height distribution by selecting the largest pulse height in a single plane. Notice that these distributions at moderate high voltages are symmetrical ; they are lacking the high energy Landau tail (see also Fig. 5-9 for Xenon and Uranium). This feature has been observed previously and was explained by Badhwar et al. [10] as arising from the loss of signal carried away by the high energy δ-rays , and was confirmed by Nagata et al. [8] for Argon and Iron beams. The pulse height distributions of δ-rays thus rejected are shown in Fig. 5-8(c).

Fig. 5-8(d) shows scatter plots between wire number(x-axis) and pulse height(y-axis) after selecting events in which beam hits wire 11 determined by MWPC. The pulse height due to the heavy track stands out as the largest pulse when evaluated event by event, even if two components are almost overlapping each other. At the highest voltage (-1.5KV for Iron), the probability of misidentifying the cell containing the primary track is ≈3%.

The most probable pulse height for the cell containing the primary track is shown in Fig. 5-10 as a function of high voltage and particle charge. For a given high voltage,the pulse height is roughly proportional to $Z^{1.5}$. It seems to be caused by saturation effect in a cell containing the primary track. If there is no saturation effect, Fig. 5-8(d) should all look similar. However, we can see more suppression of the gain in a cell containing a primary track compared with one containing δ-rays. We can see the same saturation effect in Fig. 5-7 for different ions at the same HV setting, since the angular distribution of δ-rays should be constant except the magnitude depending on the particle charges. This saturation effect seems to be the most serious problem when the chamber is operated in the very wide dynamic range.

The pulse height resolution for iron tracks from a single cell measurement (1 cm thick P10 gas) is 20 % FWHM at the lowest voltage tried (-1.1KV). This resolution can be improved by averaging 12 independent measurements in the chamber, since the pulse height distribution of a single cell is known to be symmetric. After the averaging, we obtained factor of two improvement in the pulse height resolution. This corresponds to a charge resolution of σ_z =0.8 charge units for Z=26. This indicates the rough determination of particle charges without other detector system.

5.3.3. Pulse height distribution of light ions ($1 \leq Z \leq 10$)

Unlike the very heavy ions, fast light ions produce a few δ-rays per unit length along the track. These δ-rays could deposit as much energy in a neighboring cell as the primary track in its cell. This causes a problem in a simple track finding algorithm discussed above when the largest pulse height is used to locate the cell hit by the primary beam. Such δ-rays can also make a big pulse in the same cell as the primary track which even the CFD can not overcome, since the CFD is triggered by the largest pulse within 250 nsec.

Pulse height distributions for several light ions are shown in Fig. 5-11 without(a) and with(b) selecting the largest pulse in the plane. Pulse height distributions with a high energy tail can be seen up to Z=10. The separation between primary tracks and spurious background hits is not good below Z=5 if we use a simple algorithm based on the pulse height. Fig. 5-11(d) is a plot of distance (as determined by the MWPC) versus TDC using pulse height selection. All the points far from the line are the result of choosing the wrong cell using this simple method or triggering on a large δ-ray signal by mistake. The probability of such a wrong choice ranges from 2 % for Z=1 to nearly 0 % for Z=10.

In conclusion, the simple pulse height selection technique to locate the cell containing the heaviest track among many other tracks works in most cases with less than 5 % misidentification probability per plane. This simple method is used extensively to calibrate time-to-distance relation which will be described in the next chapter.

5.3.4. Position dependence of pulse height

Due to the cell geometry and the effect of the guard planes, the position dependence of the pulse height is quite uniform at moderate high voltage settings : ≈5 % in the worst case. The uniformity also depends on the high voltage. It is likely that the change in the gain is caused by the time spread of the ionizing electrons (from the primary track and also δ-rays) into the anode; an earlier avalanche tends to suppress the gas gain of late ionizing electrons.

At higher voltages for ions between iron and uranium, we observe a jump in a pulse height by a factor of two or more when the particle passes within 0.5 mm from the anode, causing high energy tails again. Although the existence of the semi-Geiger pulse may explain these phenomena, this effect is not yet fully understood.

5.4. Position resolution and time-to-distance relation

5.4.1. General characteristics

The time-to-distance (drift time to drift distance) relation of the drift chamber was studied by using the MWPCs to determine the position of each track through the first S plane. The pulse height information was used to select the cell containing the heavy track. Several general features are as follows:

(a) The space-time relation for a given high voltage depends on the particle charge as shown in Fig. 5-13. Not only the time offset but also the shape of the space-time relation is a function of the particle charge. The drift time on the anode is shown in Fig. 5-14 as a function of the particle charge. A time shift of 110 nsec for the same drift distance is observed between Z=5 and Z=92.

(b) The drift time spectra from heavy ions and from δ-rays are quite different as shown in Fig. 5-12.

Effect (b) and part of (a) can be understood empirically considering the time slew depending on the pulse height as shown in the Fig. 3-3. However, we can not fully understand why the time-to-distance relation depends on the particle charges at the same HV setting.

(c) The position resolution becomes worse at higher voltages for high Z's as already shown in the Fig. 5-8(e). The resolution is noticeably worse at longer drift distances for $Z=92$ due to the abundance of δ-rays adding to the leading edge of the pulse. Notice that there is a tendency to trigger early (i.e. higher TDC value) far from the anode at the highest voltage as shown in Fig. 5-8(e). In these cases, the front end picks up the wrong signal from the background and the true signal from the core ionization is blocked, although the pulse height information can provide the cell containing the primary beam.

5.4.2. Single-wire position resolution and Optimum operating conditions

Before attempting to parametrize the time-to-distance relation, the single wire position resolution of one S-plane was studied in the middle of the cell as a function of high voltage and particle charges. The heavy ion tracks in the first S plane are located from the two 1mm-spacing MWPC's at 5mm from the anode wire. The position resolution is calculated from the width of the TDC spectrum using local drift velocity at this point. The resolution is estimated by subtracting the resolution of the MWPC. RMS position resolution are shown in Fig. 5-15. This estimate provides a lower limit of the intrinsic position resolution, since the effect of multiple Coulomb scattering in the gas(1.3 meters of P10 gas and 1.2 meters of air), wires and windows is still included. There is an optimum operating high voltage for any given charge and the position resolution at that voltage is very close to the multiple scattering limit. The position resolution is worse for particles with higher charges at the same voltage.

It is clear that there is no single high voltage setting where the chamber is fully sensitive between $Z=1$ and $Z=92$ with good position resolution. Our technique depends on two separate facts: (1) ADC information is used to locate the cell containing the heaviest ion track assuming that the pulse height of the heaviest ion track among other tracks is the largest in a plane in the event. (2) The CFD picks up the largest pulse within 250 nsec in a cell for light ions, and picks up the centroid of the pulse for heavy ions.

Although the first item is satisfied with less than 5% ambiguity , the CFD tends to be fired by background pulses and hence block the real timing signal of core ionization. This fact put a practical limit on the dynamic range of particle charges. In addition, number of data (hits) to be transferred to the computer becomes quite large even from this small prototype chamber when we need a large dynamic range.

There are several features which influence the choice of the high voltage depending on the dynamic range of particle charges and the position resolution required.

(a) It is necessary to operate the chamber at -1.6 KV for singly-charged minimum ionizing particles in order to have good position resolution, even though the efficiency reaches 100% at -1.5KV.

(b) The chamber is sensitive to all particles at -1.5KV. But the practical range is between Z=1 and Z=26 with poor position resolution ($\geq 600\mu$m) at both ends.

(c) The high voltage setting of -1.2 KV seems to be a good choice for heavier ions, having high efficiency between Z=5 to Z=92 with 400μm resolution in the worst case.

In conclusion, we could not find a way to operate the chamber sensitive to particles from Z=1 to Z=92 with sufficient position resolution. The practical dynamic range of particle charges at any one voltage setting turns out to be less than $\approx$ 400 in terms of Z^2.

5.4.3. Estimate of double track pair resolution

All the results so far assume that the drift chamber is hit by a single particle per event or we only need to find the track with the largest charge among many other tracks. The dynamic range studied in the previous section means the capability to locate different kinds of particles with a given high voltage but in separate events. Next, we have to study the capability of locating multiple tracks with many different charges in the same event. An obvious difficulty comes from the large amount of energy deposited into the neighbouring cells by δ-rays associated with a heavy particle. The pulses from these background δ-rays might disturb the detection of other tracks from smaller charges.

Since we did not have real multiple track samples in the beam test, we estimated the double track pair resolution using the pulse height distribution of δ-rays associated with a single heavy-ion track. First we measured the energy deposit by δ-rays as a function of the distance from the track. We assume that it becomes possible to locate the second track if the pulse height of the second track is larger than the average δ-ray signal associated with the first track. The minimum charges detectable are estimated in this way as a function of the distance from the first track. In the estimate, we use the average value of pulse height distribution, even though the pulse height distribution of δ-rays has an exponential shape.

Fig. 5-16 shows the estimate. At -1.2 kV where the chamber is sensitive to particles from boron to uranium, second boron track can be located at 9cm, 4cm and 2cm away from the track of Uranium, Xenon and Iron, respectively. At -1.5 kV where the chamber is sensitive to all particles, protons can only be located more than 20cm away from the xenon track. Even then, it is not clear how the timing signal of the second (and lighter) fragment will be effected by the presence of background δ-rays associated with heavier fragments.

6. Analysis of the ^{40}Ar projectile fragmentation

In this chapter, we will describe briefly the analysis procedure of the prototype drift chamber used in the measurement of projectile fragments from the fragmentation of $^{40}_{18}$Ar nucleus at 1.65 GeV/nucleon. During the measurement, the high voltage of the chamber was set at -1.3 KV. Through all the following calibrations, MWPC information and pulse height selection were used extensively.

6.1. Drift-time to drift-distance Parameterization

From the previous discussions, it is most important to parameterize the time slew effect (shown in Fig.5-14) and the charge-dependent space-time relation (shown in Fig.5-13) before passing data to track finding routine. There are two factors which will effect the timing of CFD, hence the position resolution of the system.

(1) Rise time of the non-linear amplifier depending on the absolute pulse height into the non-linear amplifier.

(2) Variation of pulse shape due to variations in δ-ray's contribution to the heavy ion pulse, depending on the charge of the particle.

Practically speaking, these two effects are coupled together due to the finite pulse height resolution. In addition there existed factor of two gain variation in some frontends, which introduced a 20 nsec shift in drift time even for a same charge. This also makes a separation of these two effects difficult as a function of the real charge of the particle. As a compromise, we correct these effects in two separate steps just depending on a pulse height of each wire ; (1) time slew correction and (2) charge-dependent time-to-distance parameterization. Related problem should be emphasized here that the pulse height uniformity of test pulses into frontends is quite important in order not to have time offset variations during external auto-trim adjustment of the LRS 4290 TDC system.

Firstly, raw drift time spectrum is shifted depending on a pulse height of each wire for the pulse height dependent time-slew effect. Fig.6-1 shows a TDC value at zero drift distance as a function of a ADC value. The magnitude of time slew is 80 nsec between 40 channel($Z \approx 5$) and 200 channel($Z \approx 18$). This value is consistent with the measurement using test pulse as already shown in the Fig.3-3. The rise time correction except the very low end is $\delta T = A_c/\mathrm{ADC}$, where A_c is a correction coefficient and ADC is a raw pulse height.

Time-to-distance relation after the time slew correction should reflect , more or less, the effect of δ-ray's contribution to the pulse shape. Fig.6-2 shows the relation for two different pulse height region. Solid line and dashed line corresponds to the time-to-distance relation at 30 channel($Z\approx4$) and 100 channel($Z\approx10$) respectively. There is a tendency that the average drift velocity is slower for larger pulse height, which is consistent with the tendency in the Fig.5-13. Average drift velocity is 21.1 nsec/mm for $Z\geq10$ and 17.2 nsec/mm for $Z\approx4$. We also notice some kind of saturation effect ; space-time curve at 100 channel($Z\approx10$) and 200 channel($Z\approx18$) has very small difference. Since we could not understand these effects, a two dimensional table lookup method is used to get the drift distance from the slew-corrected drift time empirically. Incident angle dependence on the space-time parameterization was not taken into account, since the angular variation in the chamber is less than ±2 degrees in our case.

This method is a very rough approximation. However it has the great merit that it does not require the charge of the track to be determined by another detector system for TDC correction, ie. all the correction can be done using the drift chamber data itself even for a multiple track event.

6.2. Track Finding

It is necessary to find multiple tracks under the actual experimental condition, apart from the simple method to find a track of the heaviest particle using ADC information as described in section 5-3. The track finding algorithm depends very much on the experimental setup and also on the configuration of the drift chamber. Firstly, our drift chamber was designed to be used in a magnetic field free region. In this case, we can assume that there is little or no curvature of the track in the chamber. Secondly, the idea of "distributed" drift chamber was initially introduced for easier straight track finding (or curved track in a homogeneous magnetic field), without using local Dalitz conditions among different projections like our old drift chamber (see appendix 1).

Firstly, the track finder program looks for straight track using the information of S-planes (vertical wires) using tree-search method. After finding the track in a horizontal projection, the program continues to find the straight track in a vertical projection from T-planes(+60degrees) and U-planes (-60 degrees) using the horizontal position of the track from the first stage. Then it fits the straight line through all the points in the track candidate. In this procedure, some care has been taken to arrange the data so that the search procedure is efficient. In order to speed up the procedure, limits are placed on the angle of the incoming track so that the time will scale as the factorial of the local density of hits and linearly with the number of tracks. Otherwise, the time will scale approximately as the factorial (this number of combination is unrealistic in our case) of the average number of wires that fire in a plane. The pulse height information also helps to reduce the number of combinations by rejecting the data of δ-rays.

Firstly, this method is applied to data of $_{54}$Xe track at -1.2 KV, which has one hit from beam and additional $\approx$ 10 spurious hits/plane from δ-rays. During the test, we found that the program finds too many false tracks if we include 3-hit candidates for the horizontal projection as shown in Fig.6-3. It should be noted that these false candidates have excellent chi-square and can not be eliminated without losing the good candidate. This situation was greatly improved if we take only candidates with 4 plane hits or pulse height cut is used. It indicates that it is necessary to have more redundancy for the first stage of track finding in order not to lose the track finding efficiency. The larger drift chamber being built for the HISS facility has 7 vertical planes following this experience. The time taken for the track finding is $\approx$ 200 msec CPU time using a VAX780 in this case.

We also studied the overall efficiency including the chamber efficiency and the track finding efficiency as a function of particle charges using $^{40}{}_{18}$Ar projectile fragmentation data at the operation voltage of -1.3 KV which is optimized for $^{137}{}_{57}$La. Fig.6-4 shows the overall efficiency of the chamber as a function of the charge of the fragment. The lower cutoff is consistent with the digital threshold of 2280 ADC system at 25. We expect that the efficiency plateau will continue to Z=57 with better position resolution.

6.3. Position Resolution

After all the corrections described in the previous sections, final position resolution was studied at the operating voltage of -1.3 KV. Fig.6-5 shows a scatter plot between deviation from the fitted track (Y-axis) and drift distance (X_axis) for fragments between Z=10 and 18. Distributions of the deviation are shown in Fig.6-6 for several charge regions. The position resolution (standard deviation) decreases monotonically from 400μm to 250μm as a function of fragment charges between Z=3 and 18 as shown in Fig.6-7. Fig.6-8 shows a position resolution as a function of drift distance for fragments ($10 \leq Z \leq 18$). Above resolutions are not corrected for the deviation from the straight line (estimated to be $\approx$500μm over 110cm of path length) due to the fringing magnetic field (50 to 150 gauss) from the HISS dipole.

7. Other tracking detectors for high-energy heavy-ions

During our studies, we have noticed several drawbacks when drift chamber is applied to highly charged projectiles in the GeV/nucleon energy region. In this section, we would like to discuss other possible tracking detectors for high-energy heavy-fragments.

The main problem in the present drift chamber seems to be caused by

(1) Saturation of gas amplification.

(2) Long range of δ-rays in chamber gas.

Although operation of the present drift chamber in the magnetic field will solve most of the problems associated with item (2), high track density downstream of the target in high-energy nucleus-nucleus reaction prevents us to use this technique. We might have two possible ways to overcome these difficulties in the future.

The saturation of gas amplification makes pulse height separation between δ-rays and the core ionization worse at higher voltages (or at higher gas gain). One possible way to improve this is to operate the drift chamber in the ionization mode which does not utilize any gas amplification mechanism. Three-dimensional-MUSIC detector (Multiple Sampling Ionization Chamber) being constructed by a collaboration between GSI and LBL [11] will satisfies most of the requirements. This is essentially a time projection chamber with two projected geometry operated in the ionization mode , as a modified version of the existing MUSIC detector [4]. The detector has good charge resolution ($\sigma_z = 0.3$ at $Z=57$) by a multiple sampling of the energy loss. It also has track information utilizing the TPC electronics in order to get the rigidity information. The position resolution of this detector was checked to be less than 200 μm for $Z=57$ [11]. On the other hand, drawbacks of this detector are (1) lower charge threshold at $\approx$ 10 due to a noise level from 2cm sampling and (2) longer detector deadtime due to longer (50cm) drift length.

Alternative way is to use denser material as detectors in order to keep the range of δ-rays short. It is clear from emulsion pictures at the Bevalac that the double track separation between heavy projectile fragment and light fragment (even for alpha particles) is quite good due to the shorter range of δ-rays compared with the size of core ionization. It is becoming popular to use a fully depleted thin Si wafer for drifting the ionization to the anode [12]. Silicon drift chamber has higher stopping power against δ-rays while being able to keep the total thickness comparable to the gas chamber ($\leq$ 300 mg/cm^2 for 1mm thick Si). It was reported that the position resolution of 20 μm can be reached. The pulse height resolution will be good, helped also by the disappearance of Landau tail for heavier ions.

The drift chamber is the best compromise for high-energy heavy-ion experiments including the detection of heavy projectile fragments at high rates, with moderate dynamic range, and with large geometrical coverage using the well established technique with several modifications as described in this paper. However the detectors mentioned in this chapter will be quite useful and suitable for some particular experiment.

8. Conclusions

In this paper, we have reported the application of the drift chamber with several novel features for the detection of heavy projectile fragments produced in nucleus-nucleus reactions in the GeV/nucleon energy range.

The prototype drift chamber can be operated with full efficiency and good position resolution (which is close to the multiple scattering limit) by adjusting the high voltage to the optimum for a given heavy ion. The combination of constant fraction discriminator (CFD) and pulse height information enables us to reject spurious hits from δ-rays very effectively. However, we could not find a single operating condition where the chamber was fully sensitive to ions from protons up to uranium with good position resolution. Instead, we found several operating conditions which could provide adequate position resolution ($\approx$ 400 micron) for limited ranges of fragment charges. The maximum dynamic range achieved in terms of Z^2 is $\approx$ 400 for any one voltage setting.

The chamber was successfully operated in the actual experiment for tracking wide range of heavy projectile fragments produced from the breakup of ${}^{40}{}_{18}$Ar beam at 1.65 GeV/nucleon. We have also established the software in addition to new hardwares.

From the prototype study, we have found that more planes with vertical wires are necessary in terms of track finding. Including these modifications, the new drift chamber (active area is 2m wide and 1.5m high with 15 sense planes) is being built for the HISS detector system at Lawrence Berkeley Laboratory.

9. Acknowledgement

We would like to give thanks to the staff of the LBL Bevalac for their cooperation during measurements, and to the INS-LBL group who let us use the secondary beam during their experiments. We also would like to give thanks to Mr's Leo Greiner, John Milburn, John Wolf, and Mel Flores for the work during the chamber construction and beam tests. This work was supported by the Director, Office of Energy Research, Division of Nuclear Physics of the Office of High Energy and Nuclear Physics of the U.S. Department of Energy under Contract DE-AC03-76SF00098.

10. Appendix : Drift chamber with foil-cathodes

During the development of the front-end circuit, a Walenta type drift chamber [7] was also studied under almost the same conditions. We will briefly report the results and a comparison between drift chambers with foil-cathodes and with field-shaping wires.

Chamber construction is greatly simplified with foil (aluminized Mylar) cathodes. The anodes (20micron Au-W wires) were operated at ground potential while the field wires (75micron Cu-Be wires) and foils were biased by two separate negative HV supplies. Figure 10-1 shows this cell structure and the resultant field structure. To improve the uniformity of the drift field, the field wires are operated 100 volts more negative than the cathodes. Larger values of dV cause increasingly large dead regions around the field wires.

Full efficiency for singly-charged minimum ionizing particles was achieved at -1.5 KV. Test results using Fe, La, and Au ($Z = 26, 57, 79$) beams at 1 Gev/nucleon were similar to those of the prototype chamber and are summarized below:

(1) Although the position resolution is comparable to that of the prototype with field-shaping wires, the space-time relation is not linear near the field wire due to the smaller electric field.

(2) The pulse height is reduced near the anode just as in the prototype but it is also smaller near the field wires due to the regions where the drift field is almost zero.

(3) When we want to operate the chamber at lower gain for heavy ions, it is necessary to decrease the high voltage of cathodes and field-wires at the same time in order not to increase the size of the dead region near field wires. As a result, it is impossible to have enough electric field for saturated drift velocity. One possible way to increase the electric field is to use thicker anode wires. However, a chamber with thicker anode wires (75 micron Au-W) showed limited-Geiger pulses from argon tracks ($Z=18$) when the high voltage was set to have full efficiency for protons (-2.1 KV with 2micro amps threshold).

(4) Experience with 200cm × 100cm chambers with 75 micron anodes [3] has shown that using aluminized mylar foil for cathode planes would be very difficult to extend to much larger chambers since any deviation from planarity causes reduced anode to cathode spacing and thus high voltage breakdown.

In conclusion, drift chambers with foil cathodes work just fine for low Z particles but are not suitable for a large dynamic range of particle charges. Furthermore, there are mechanical difficulties with making very large ones.

11. References

* Present address :
National Laboratory for High Energy Physics (KEK), Tsukuba, Japan

[1] D. E. Greiner, P. J. Lindstrom, H. H. Heckman, Bruce Cork and F. S. Bieser Phys. Rev. Lett. 35 (1975) 152.

[2] D.E.Greiner, Proceedings of the Int. Conf. on Nucleus-Nucleus Collisions, MSU, Oct 1982.
and also D.E.Greiner, Proceedings of the conference on Instrumentation for Heavy Ion Nuclear Research, Oak Ridge, TN, Oct 1984.

[3] J. P. Dufour, D. L. Olson, M. Baumgartner, J. G. Girard, P. J. Lindstrom, D.E. Greiner, T. J. M. Symons, and H. J. Crawfords, Nucl. Instr. and Meth. A241 (1985) 491

[4] W. B. Christie, M. S. Thesis, University of California Davis, 1985

[5] A. Sandoval, private communication

[6] I. Tanihata, O. Yamakawa, H. Hamagaki, O. Hashimoto, S. Nagamiya, Y. Shida, N. Yoshikawa,K. Sugimoto, T. Kobayashi, D.E. Greiner, N. Takahashi, and Y. Nojiri, Phys. Lett. 160B (1985) 380

[7] M. Simon, M. Henkel and G. Schieweck, Nucl. Instr. and Meth. 192 (1982) 483.

[8] K. Nagata, J. Kikuchi and T. Doke, Nucl. Instr. and Meth. 188 (1981) 217.

[9] B. Sadoulet and A. Litke, Nucl. Instr. and Meth. 124 (1975) 349.

[10] G. D. Badhwar, Nucl. Instr. and Meth. 109 (1973) 119

[11] W.F.J. Mueller, H. Sann, and T.Kobayashi, private communication

[12] P. Rehak, E. Gatti, A.Longoni, J. Kemmer, P. Holl, R. Klanner, G. Lutz, and A. Wylie, Nucl. Instr. and Meth. 235 (1985) 224

12. Figure Captions

Fig. 1-1 Picture of single $^{137}_{57}$La beam track at 1.3 GeV/nucleon taken with LBL streamer chamber without magnetic field. All white hairs are δ-rays with multiple Coulomb scattering in the gas. Horizontal and vertical scales are 120 and 60cm, respectively.

Fig. 2-1 Drift-cell cross section. The anode and guard wires are at the ground potential. The high voltage on i-th field shaping wire is given as $H_i = H_0 + \delta V \times (i-1)$. During this measurement, δV was fixed at -0.2KV. In the paper, H_0 is used to specify high voltage condition.

Fig. 2-2 Configuration of equipotential surfaces in a drift cell in every 40 volts.
(a) HV = -1.2 KV suitable for heavy ions between Z=5 and Z=92.
(b) HV = -1.6 KV which guarantees full efficiency for Z=1.

Fig. 2-3 The electric field in midplane of the cell at HV=-1.2KV and HV=-1.6KV.

Fig. 2-4 Schematic view of prototype drift chamber. Twelve planes are distributed with 10cm spacing over 110cm in a single gas volume of P-10 gas. Active area is 40cm wide, 30cm high and 110cm long.

Fig. 2-5 The cross section of one modular unit in the prototype chamber.
(1) sense and drift wires. (2) field shaping wires. (3) guard wires. (4) aluminum stiffener. (5) rubber gasket. (6) printed circuit. (7) G-10 frames. (8) aluminum spacer. (9) aluminum frame for guard wires

Fig. 2-6 Picture of prototype drift chamber. Active area is 40cm wide, 30cm high and 12 sense planes are distributed with 10cm spacing over 110cm.

Fig. 3-1 Functional block diagram of the front-end. Pulse shapes at several points in the circuit are also shown as expected for light ions such as carbon. The circuit picks up the timing from the largest pulse inside a 200nsec time window with a fraction of 80%.

Fig. 3-2 Complete circuit of the front-end.

Fig. 3-3 Time slew as a function of input test pulse current with constant rise time.

Fig. 5-1 Pulse height of 3 KeV and 5.9 KeV x-rays as a function of the high voltage. Broken line is a ratio of pulse height between 5.9 KeV and 3 KeV. During the measurement, δH is set at -0.3kV.

Fig. 5-3 Pulse shapes of $_{54}$Xe ion and $_{92}$U ion at several high voltages. Beam hits the chamber at 5 mm from the anode wire.

Fig. 5-4 Single plane efficiency between $_{1}$t and $_{6}$B as a function of the high voltage. Open circle is a single hit efficiency.

Fig. 5-5 The average multiplicity of wires in a single plane as a function of the high voltage for a variety of particles. The total number of wires in a plane is 20 covering a distance of 20cm on both side of the particle.

Fig. 5-6 Raw wire pattern of two MWPC's and four triplets (s, t and u) in the drift chamber without(1) and with(2) the pulse height selection for $_{26}$Fe(a), $_{54}$Xe(b), and $_{92}$U(c) at -1.2KV.

Fig. 5-7 Scatter plot of pulse height (Y-axis) vs wire number (X-axis) in the drift chamber for $_{26}$Fe(a), $_{54}$Xe(b), and $_{92}$U(c). Beam hits wire #11 selected using MWPC information.

Fig. 5-8 Data of $_{26}$Fe track through the drift chamber.
High voltages are -1.1KV(1), -1.2KV(2), -1.3KV(3), -1.4KV(4), and -1.5KV(5).
(a) Raw pulse height distribution in one plane.
(b) Distribution of largest pulse height in one plane.
(c) Pulse height distribution after removing the largest pulse in one plane.
(d) Scatter plot of wire number (X-axis) in the drift chamber versus pulse height (Y-axis). Beam hits wire #11 selected using MWPC information.
(e) Interpolated position from two MWPC's (X-axis) versus TDC of drift chamber (Y-axis) after selecting the largest pulse in one plane.

Fig. 5-9 Pulse height distributions of ${}_{54}$Xe at -1.1KV (a) ${}_{92}$U at -1.0KV (b) after the pulse height selection.

Fig. 5-10 Most probable pulse height of heavy ions as a function of
(a) the high voltage for a given Z.
(b) the charge of heavy ions for a given high voltage.

Fig. 5-11 Data for lighter ions
Rows are
(1) ${}_{1}$t at -1.6KV (2) ${}_{2}$He at -1.5KV (3) ${}_{3}$Li at -1.5KV (4) ${}_{5}$B at -1.4KV
(5) ${}_{10}$Ne at -1.3KV
Columns are
(a) Pulse height distributions without pulse height selection.
(b) Same as (a) with pulse height selection.
(c) Time-to-distance relation using MWPC information after the pulse height selection.

Fig. 5-12 Drift time spectrum of Xenon at -1.2KV
(a) without pulse height cut
(b) That of core ionization selected using pulse height information
(c) That of δ-rays selected using pulse height information

Fig. 5-13 Space-time relation at -1.2KV for ${}_{5}$B, ${}_{26}$Fe, ${}_{54}$Xe, and ${}_{92}$U with pulse height selection. Positions (x-axis) are interpolated from 1mm spacing MWPC's. Larger TDC value corresponds to smaller drift time.

Fig. 5-14 Time slew in the drift time spectra as a function of the charge of the ion. Drift time shown corresponds to zero drift distance.

Fig. 5-15 Estimated position resolution(rms) at 5mm drift length as a function of high voltage and charge of heavy ions. Data are for ${}^{3}_{1}$t, ${}^{6}_{2}$He, ${}^{9}_{3}$Li, ${}^{26}_{26}$Fe, ${}^{131}_{54}$Xe, and ${}^{238}_{92}$U ions.

Fig. 5-16 Estimated double track pair resolution. Minimum detectable charge of the second track is shown as a function of the distance from the first track at -1.2KV and -1.5KV. Dash-dot line is the lowest charge detectable for a single track.

Fig. 6-1 TDC value at zero drift length as a function of the pulse height, showing a large time slew effect . This data is used to correct the time slew as a function of the ADC value. The ADC channel at 30 and 200 corresponds to $Z\approx4$ and $Z\approx18$ respectively.

Fig. 6-2 Space-time relation after the time slew correction. Solid and dashed line corresponds to space-time relation for $Z\approx3$ (ADC=30ch) and $Z\approx10$(ADC=100ch) respectively. Average drift velocity for $Z\geq10$ is 21.1 nsec/mm.

Fig. 6-3 Three hit candidate (dotted line) and four hit candidate (solid line) from ${}_{54}$Xe track at -1.2 KV. Open circles are anode wires. Crosses are hits without solving left-right ambiguity.

Fig. 6-4 Overall detection efficiencies as a function of the charge of fragments. This includes the efficiency of the chamber and track finding efficiency.

Fig. 6-5 Scatter plot of deviation from the fitted track (Y-axis) versus drift distance in a cell (X-axis) for $10 \leq Z \leq 18$.

Fig. 6-6 Distribution of deviations from the fitted track for (a) $5 \leq Z < 10$, (b) $10 \leq Z < 15$, (c) $15 \leq Z \leq 18$.

Fig. 6-7 Overall single plane position resolution as a function of the fragment charge.

Fig. 6-8 Position resolution as a function of drift distance.

Fig. 10-1 Electric field of Walenta type drift chamber with foil cathodes.

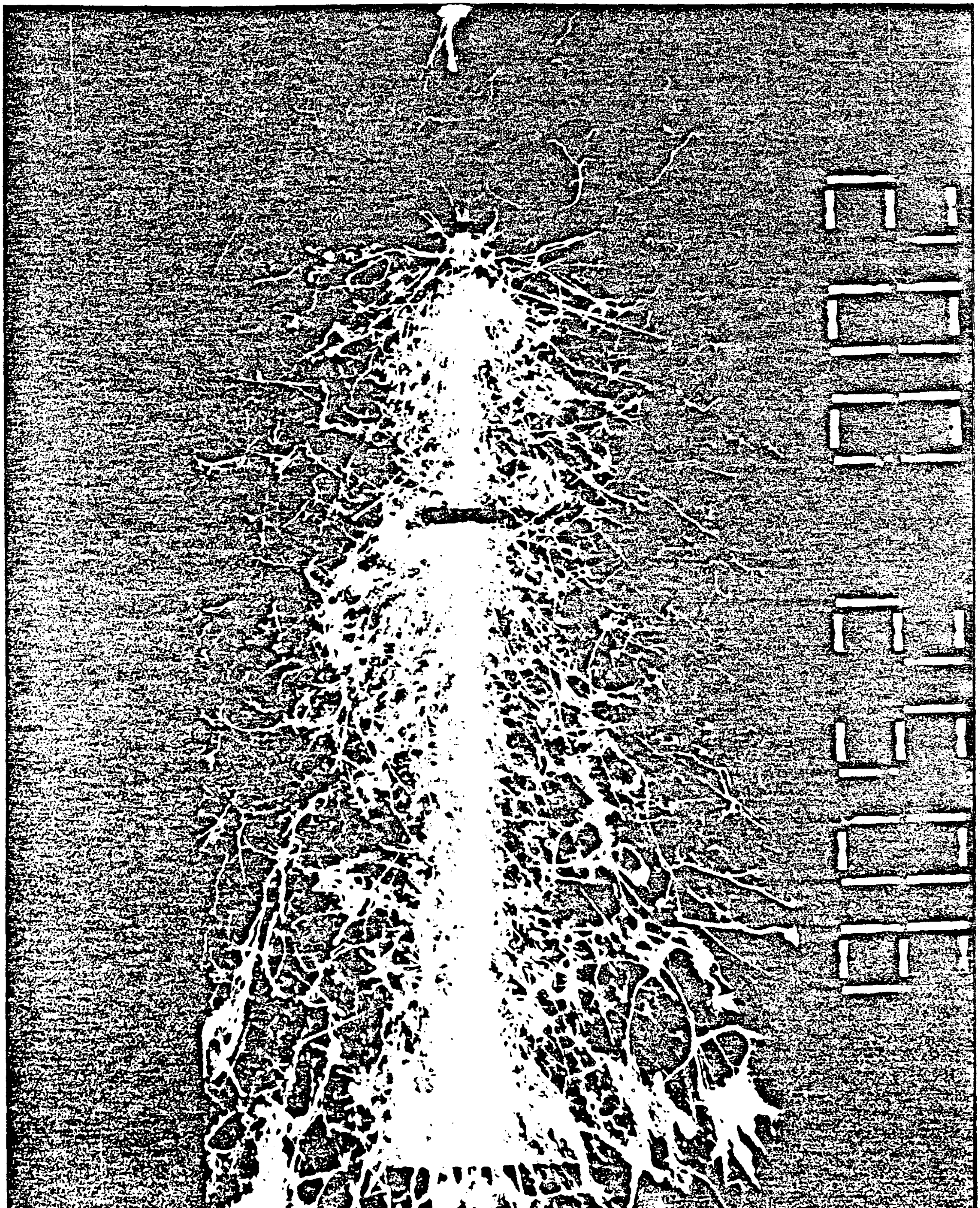

Fig. 1-1

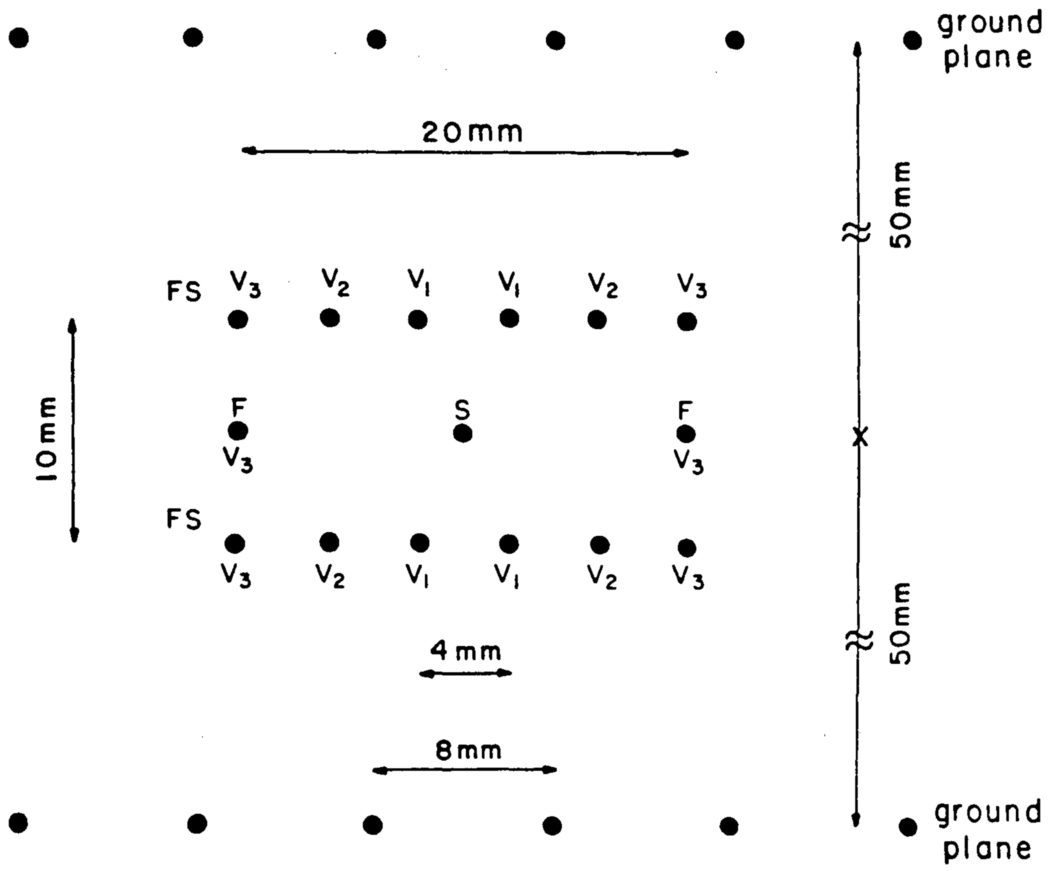

XBL 869-3290

Fig. 2-1

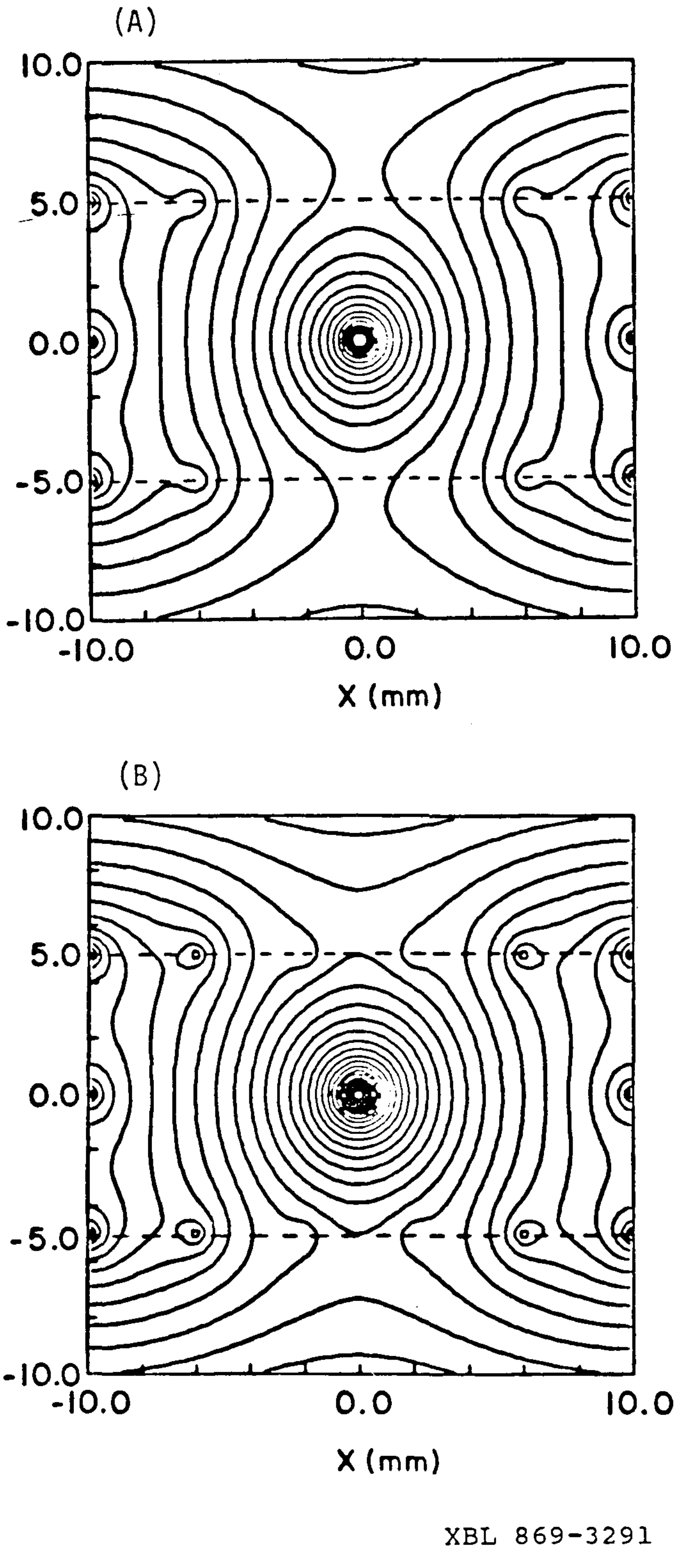

XBL 869-3291

Fig. 2-2

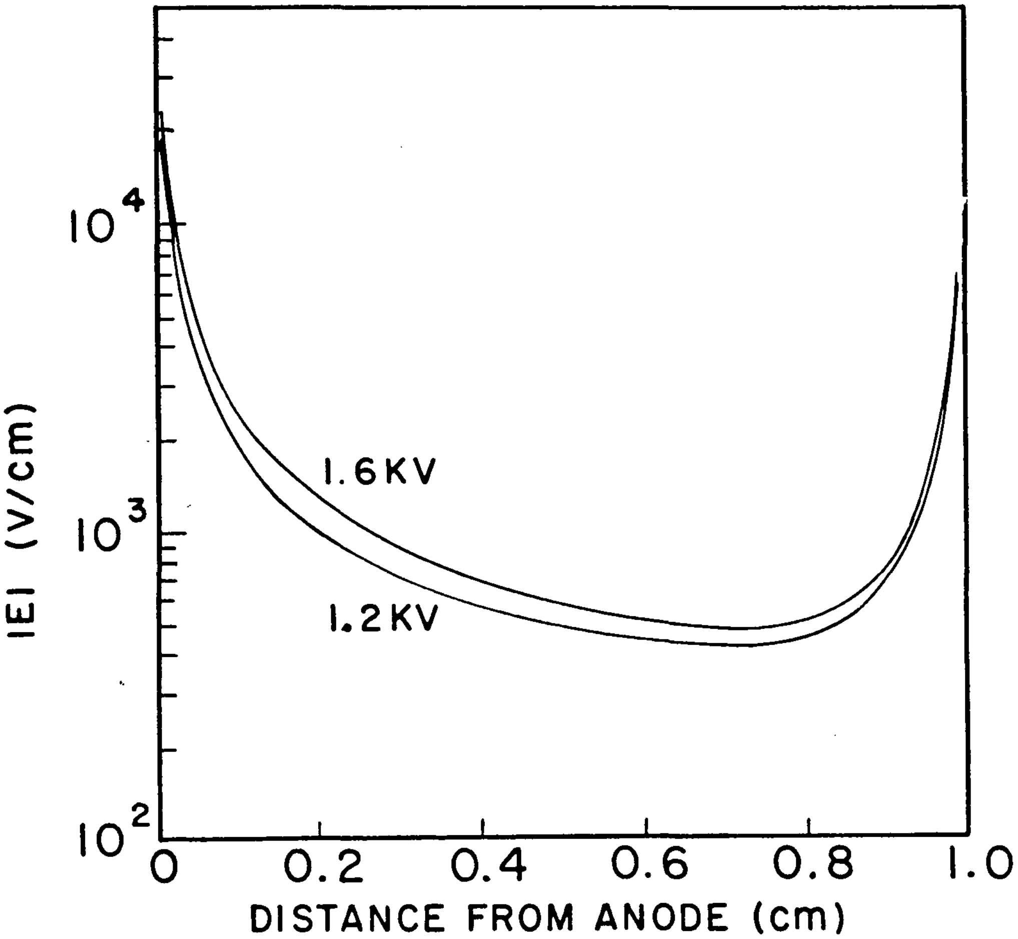

XBL 869-3310

Fig. 2-3

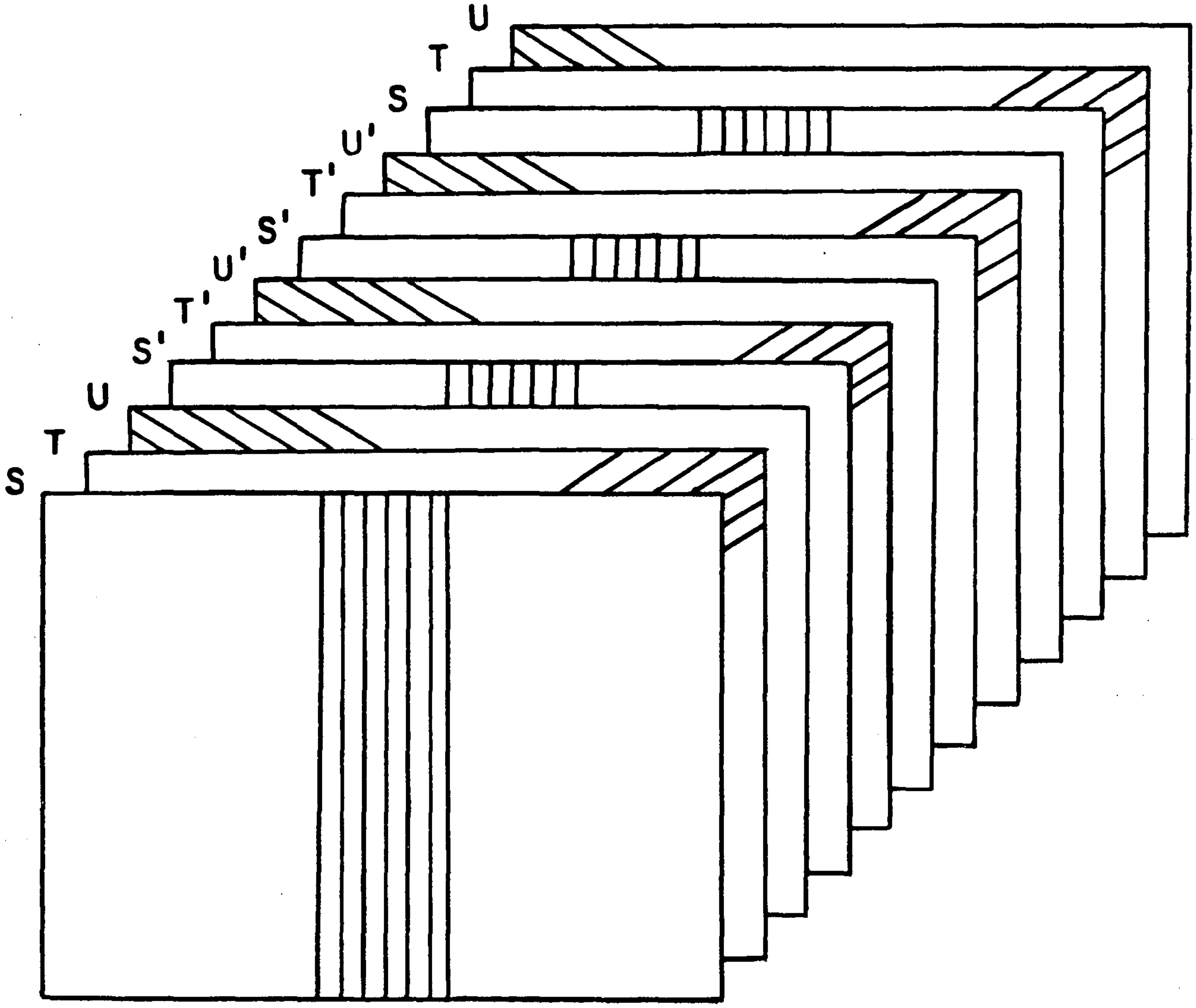

XBL 869-3309

Fig. 2-4

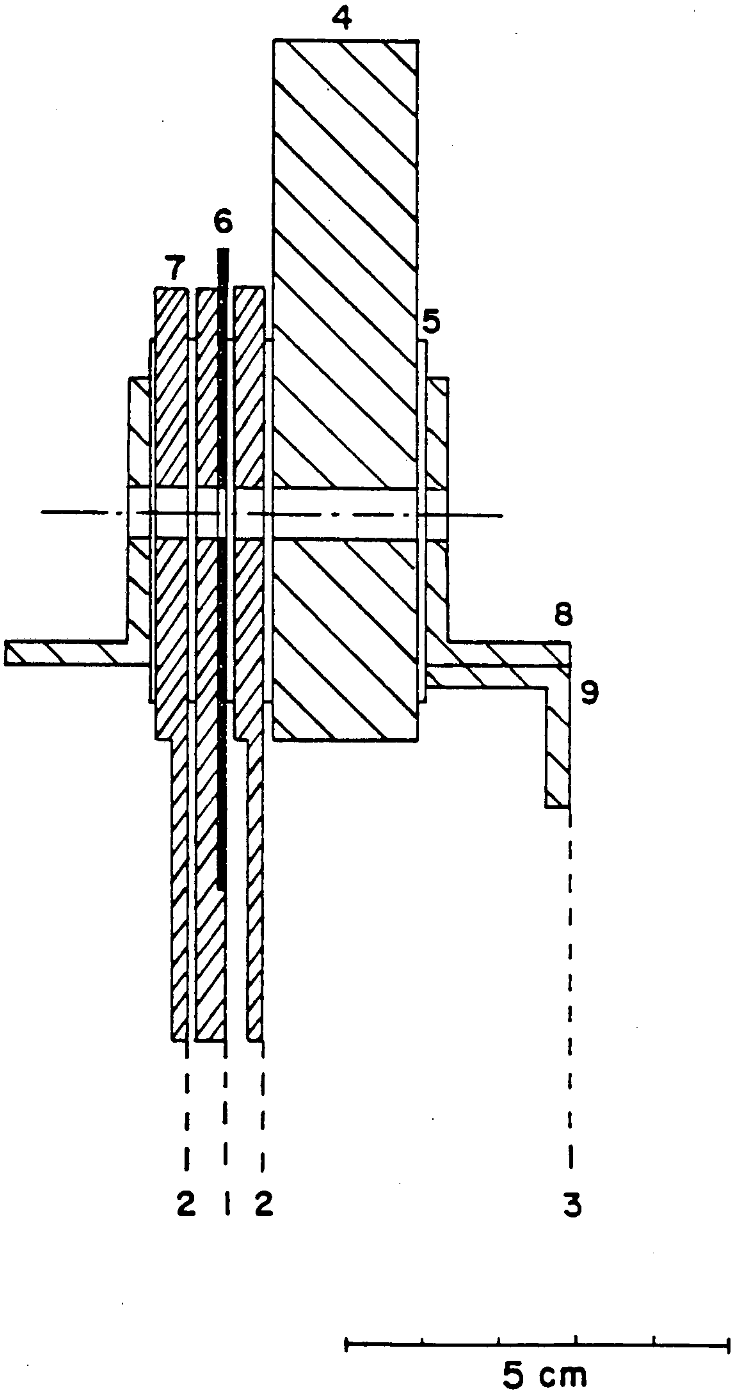

XBL 869-3301

Fig. 2-5

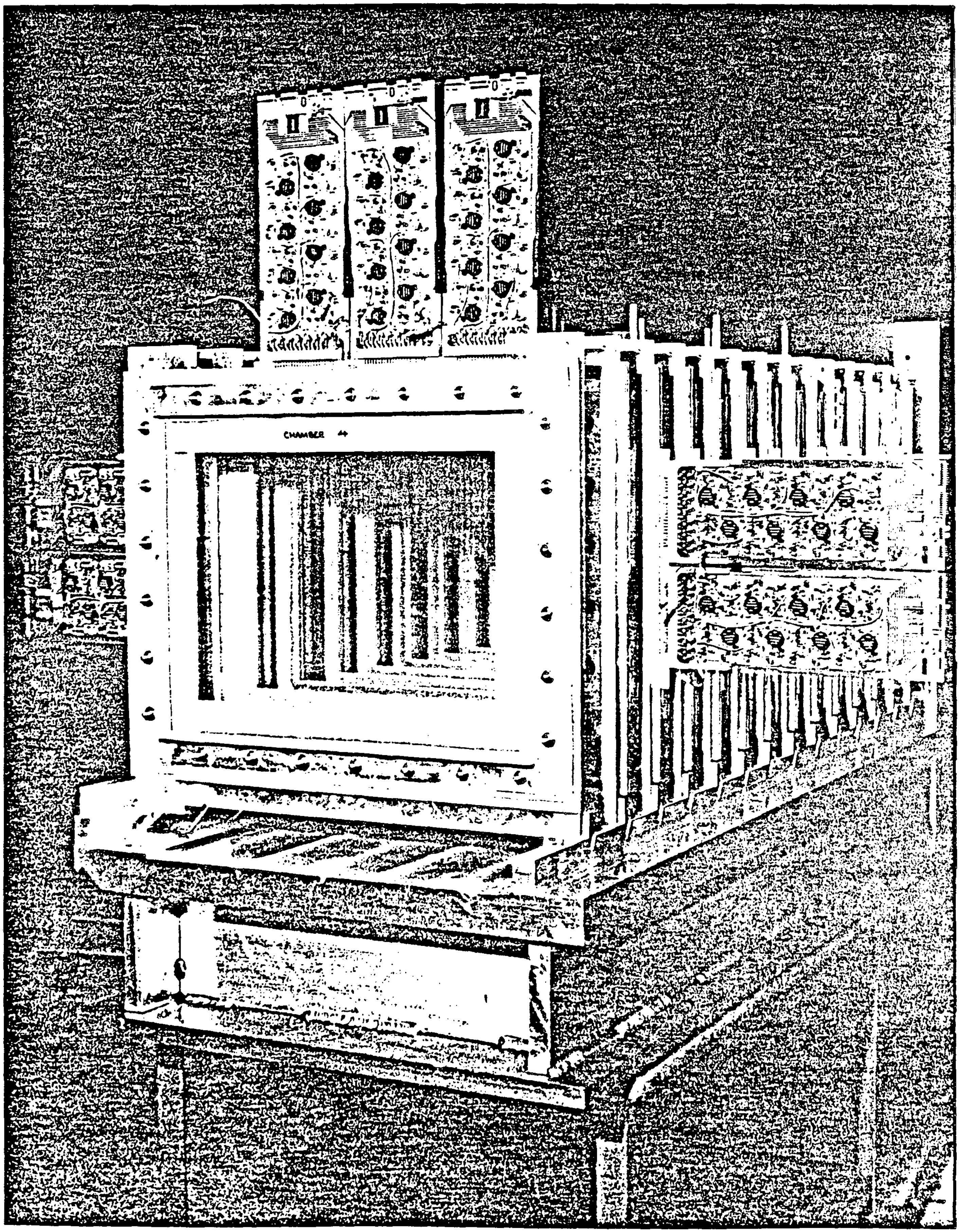

Fig. 2-6

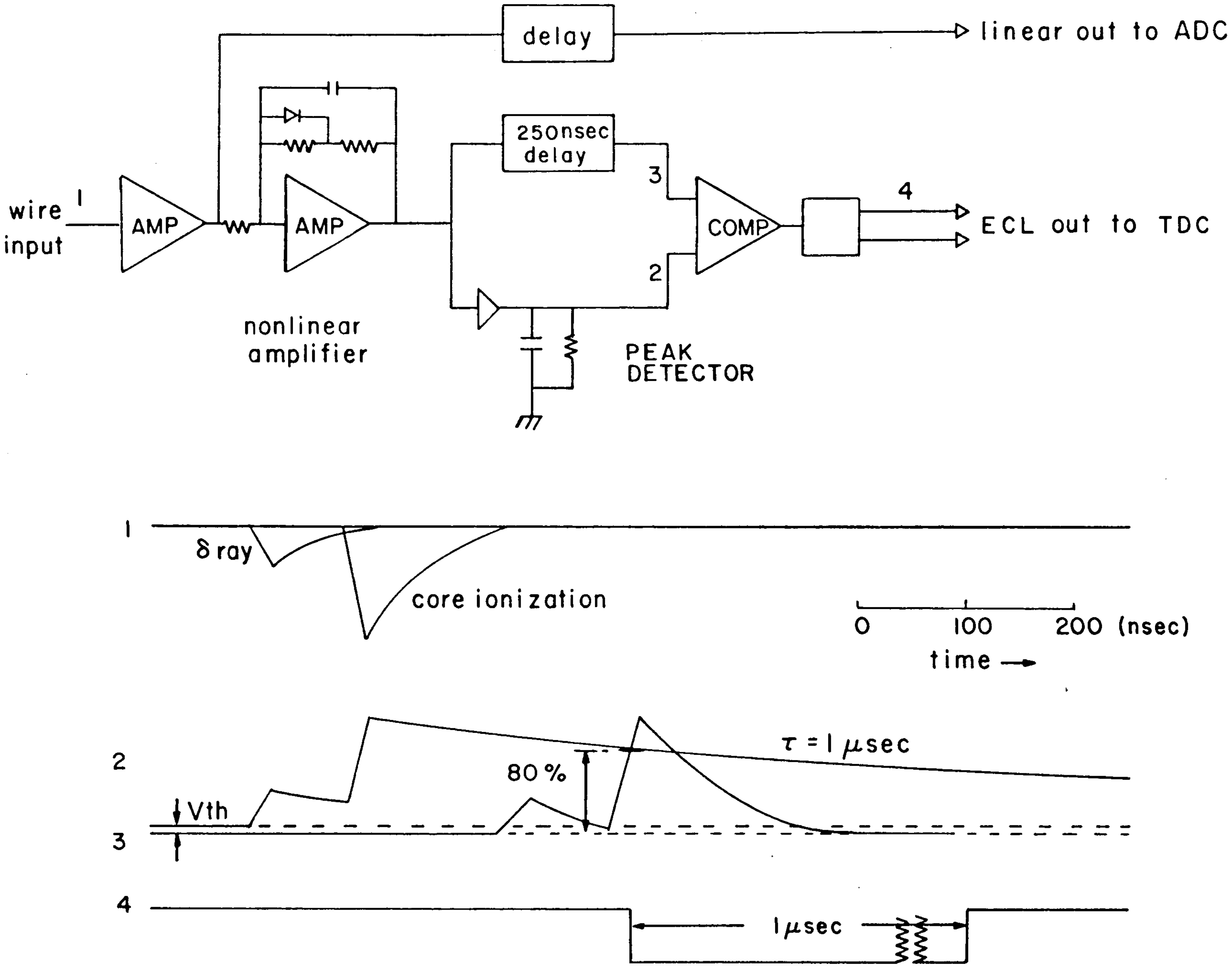

Fig. 3-1

XBL 869-3312

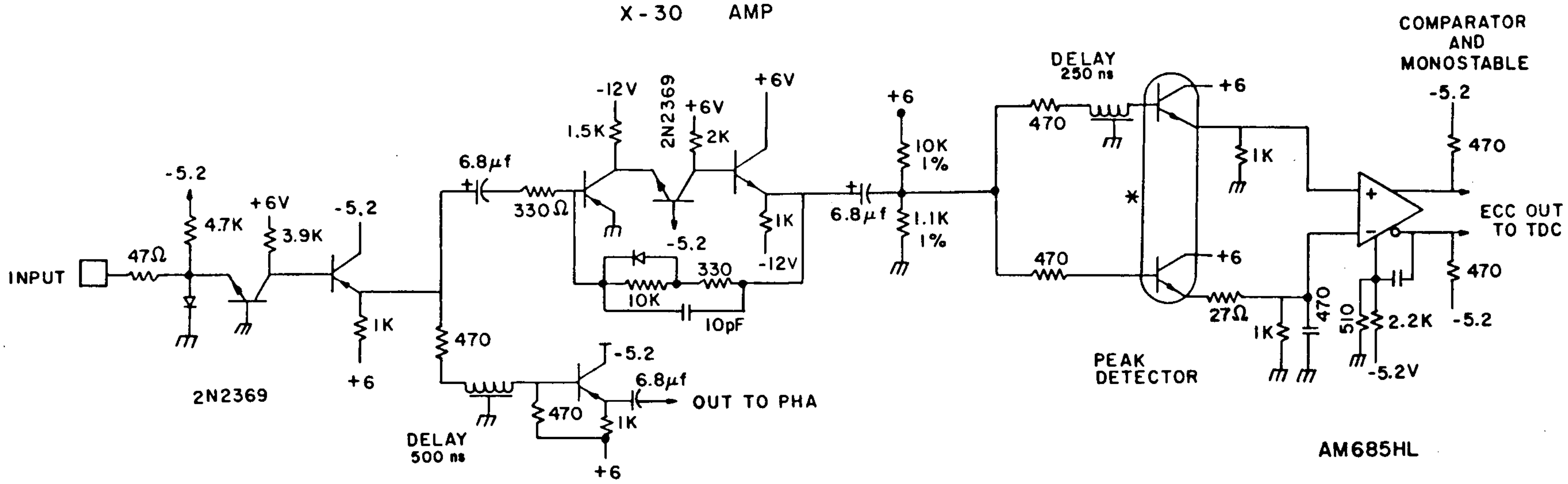

XBL 869- 3318

Fig. 3-2

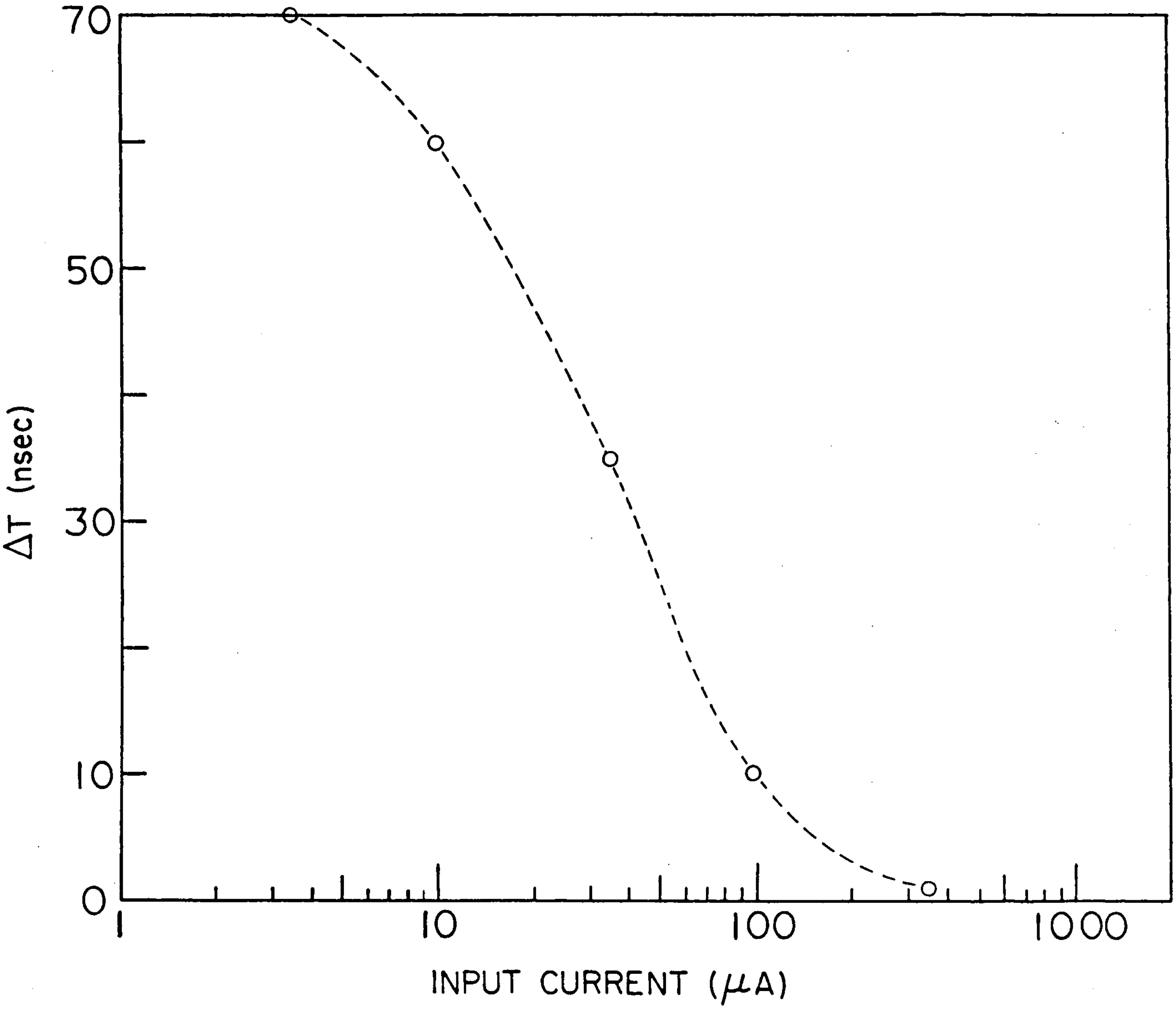

XBL 869-3311

Fig. 3-3

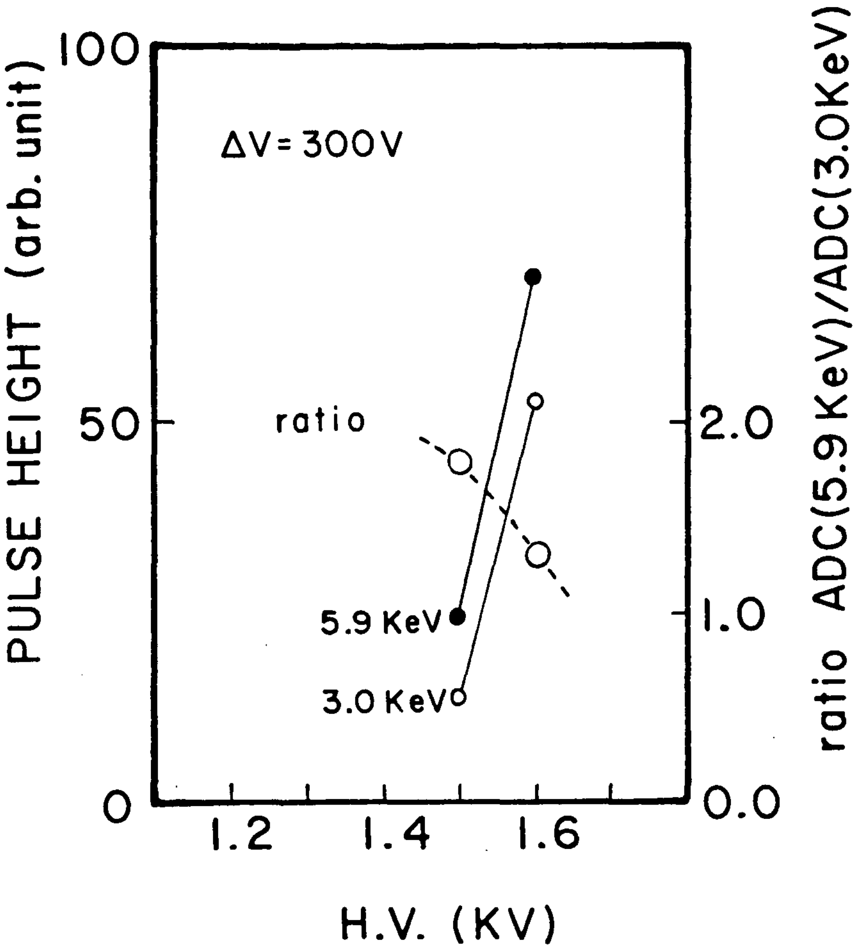

XBL 869-3295

Fig. 5-1

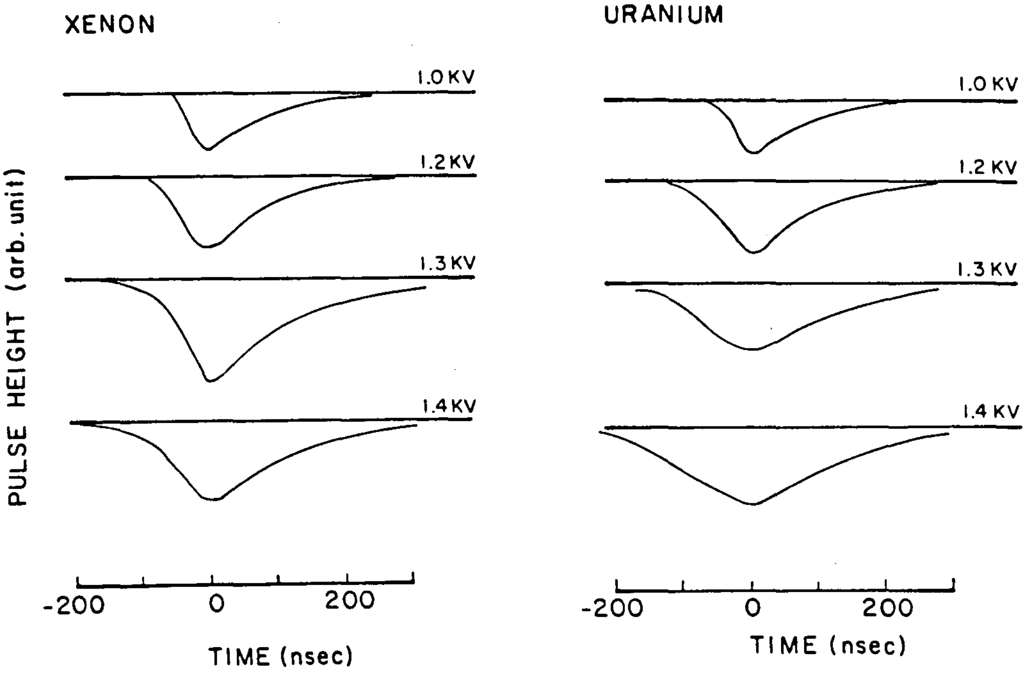

XBL 869-3292

Fig. 5-3(a)

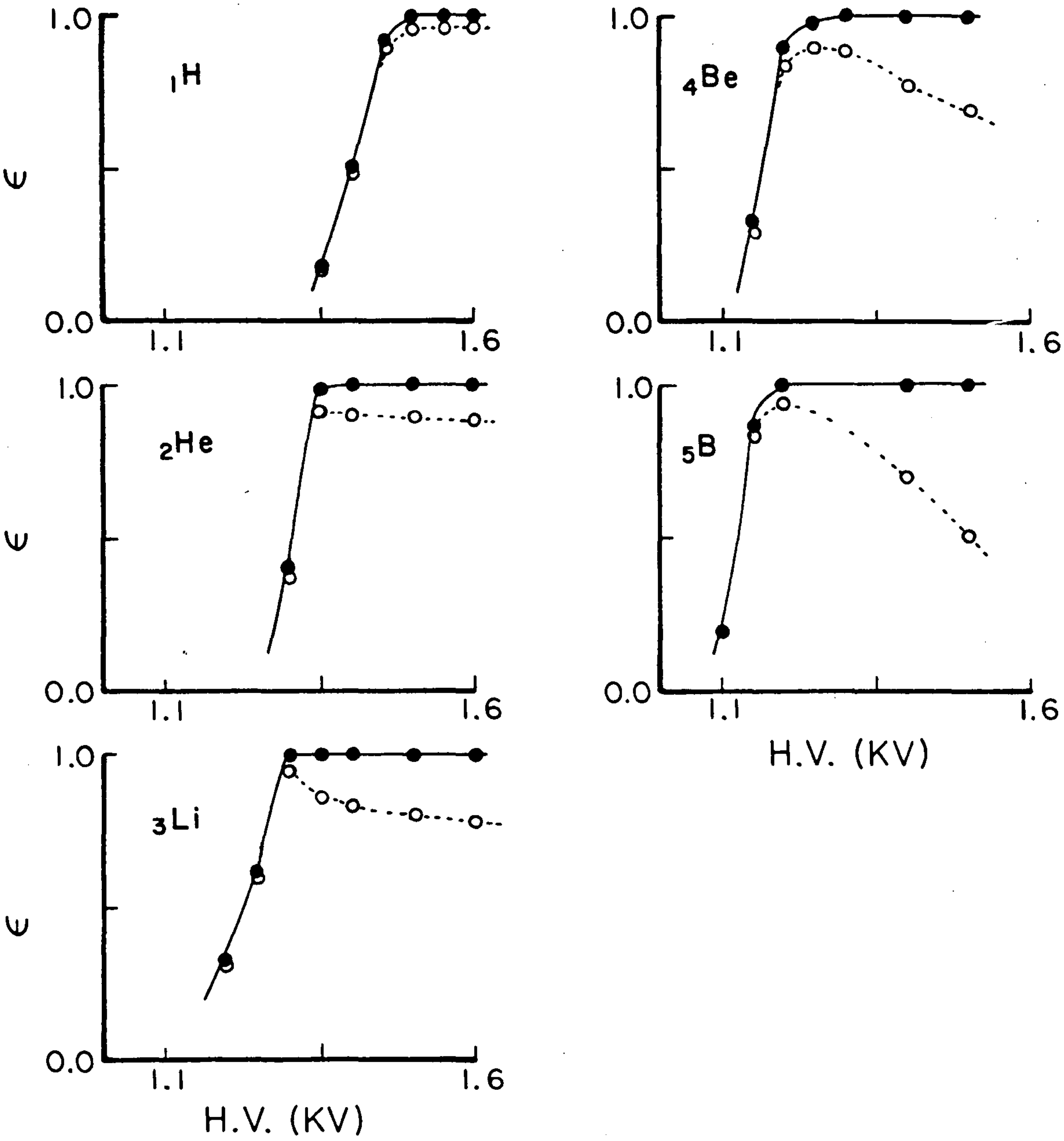

XBL 869-3293

Fig. 5-4

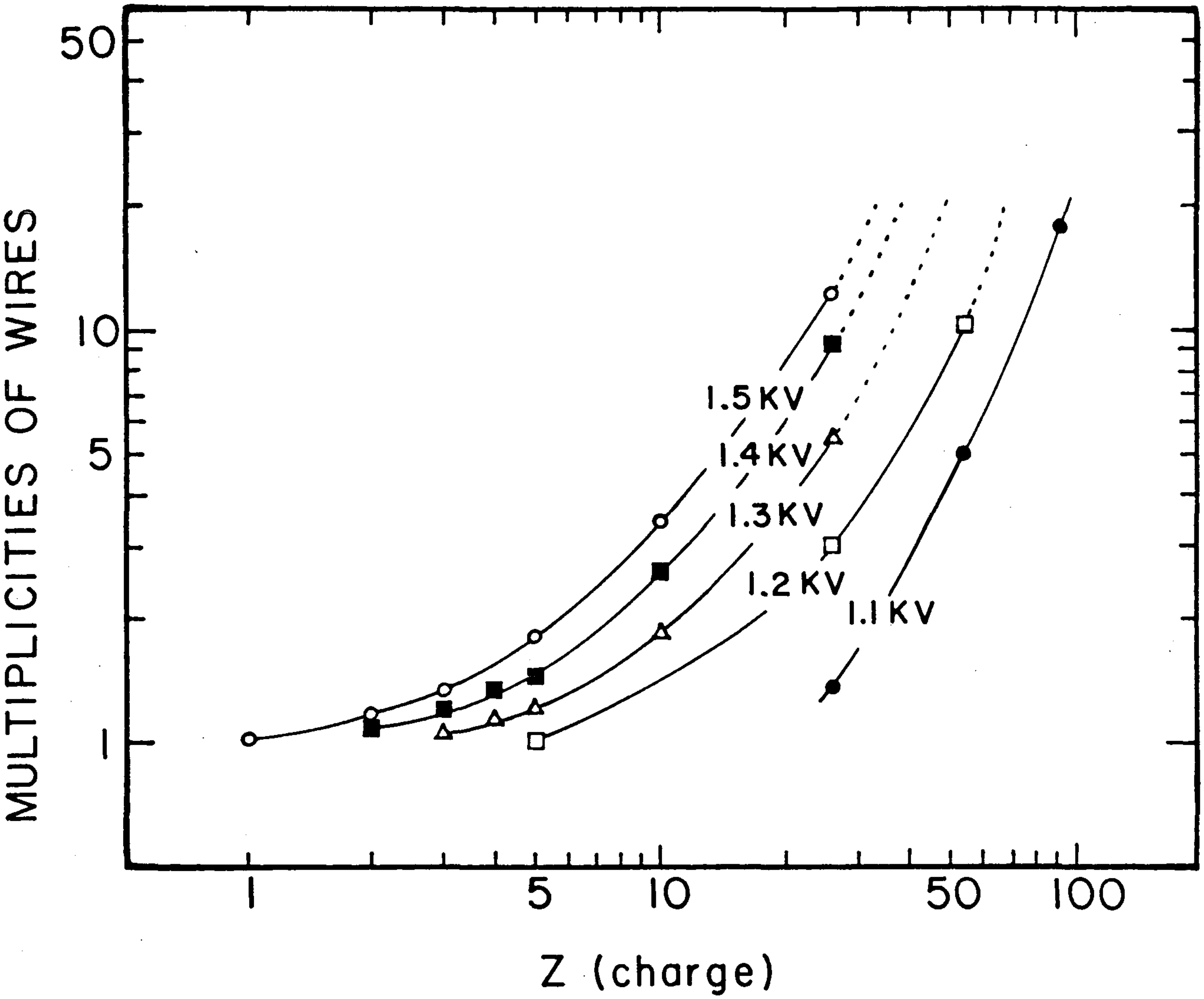

XBL 869-3314

Fig. 5-5

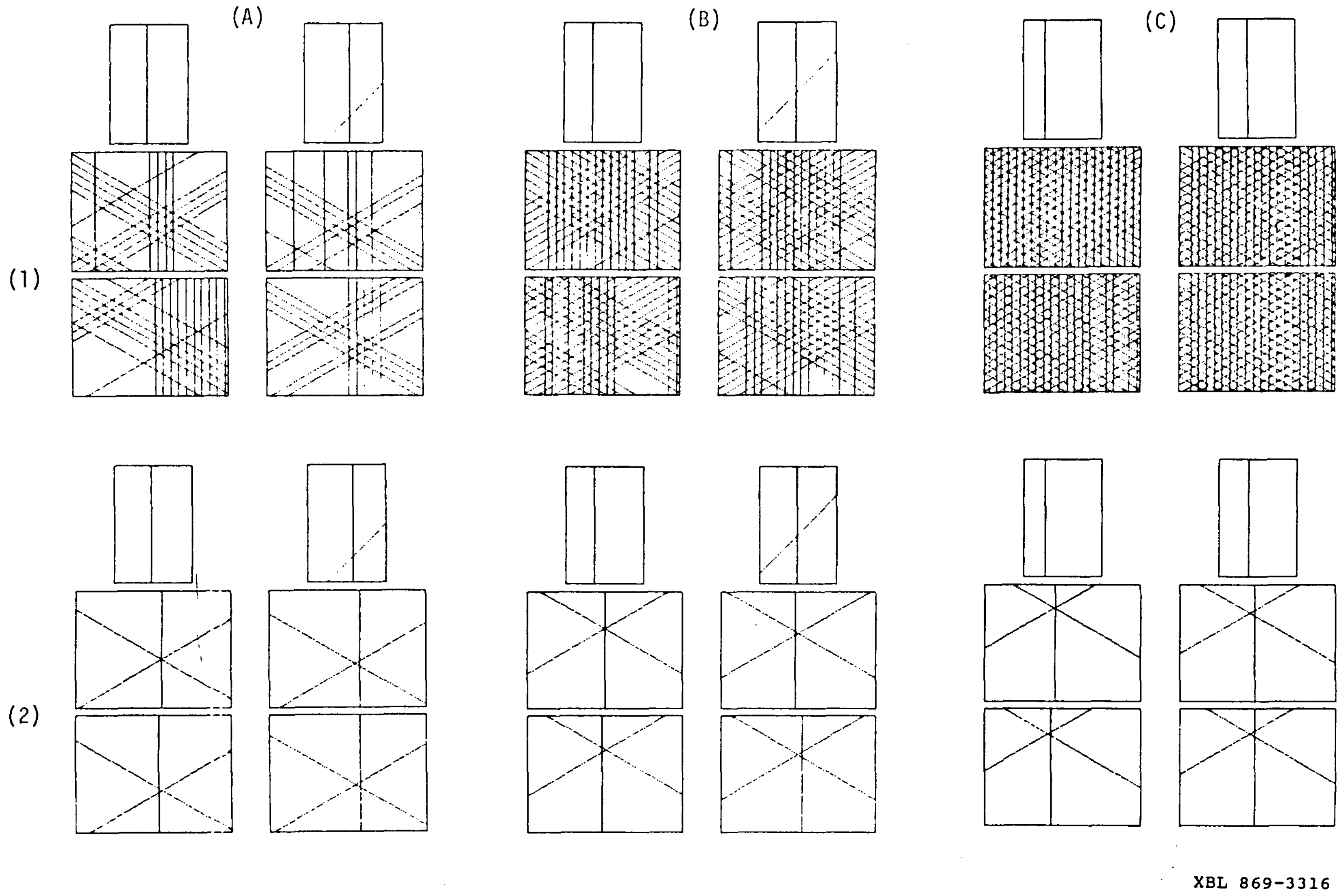

Fig. 5-6

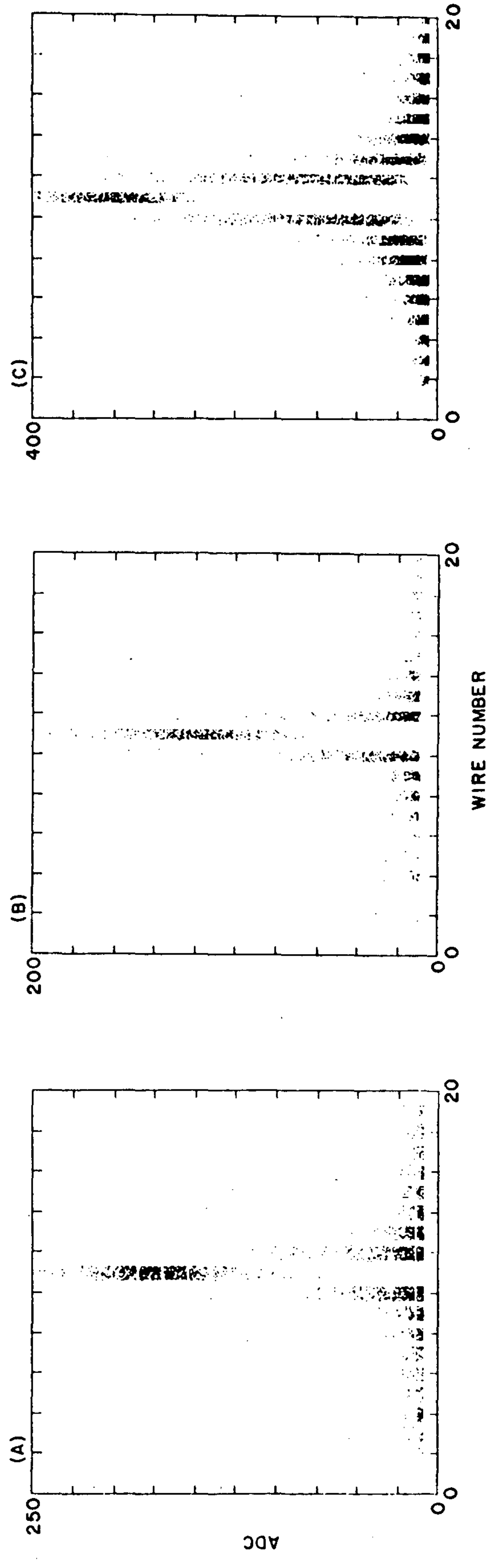

XBL 869-3304

Fig. 5-7

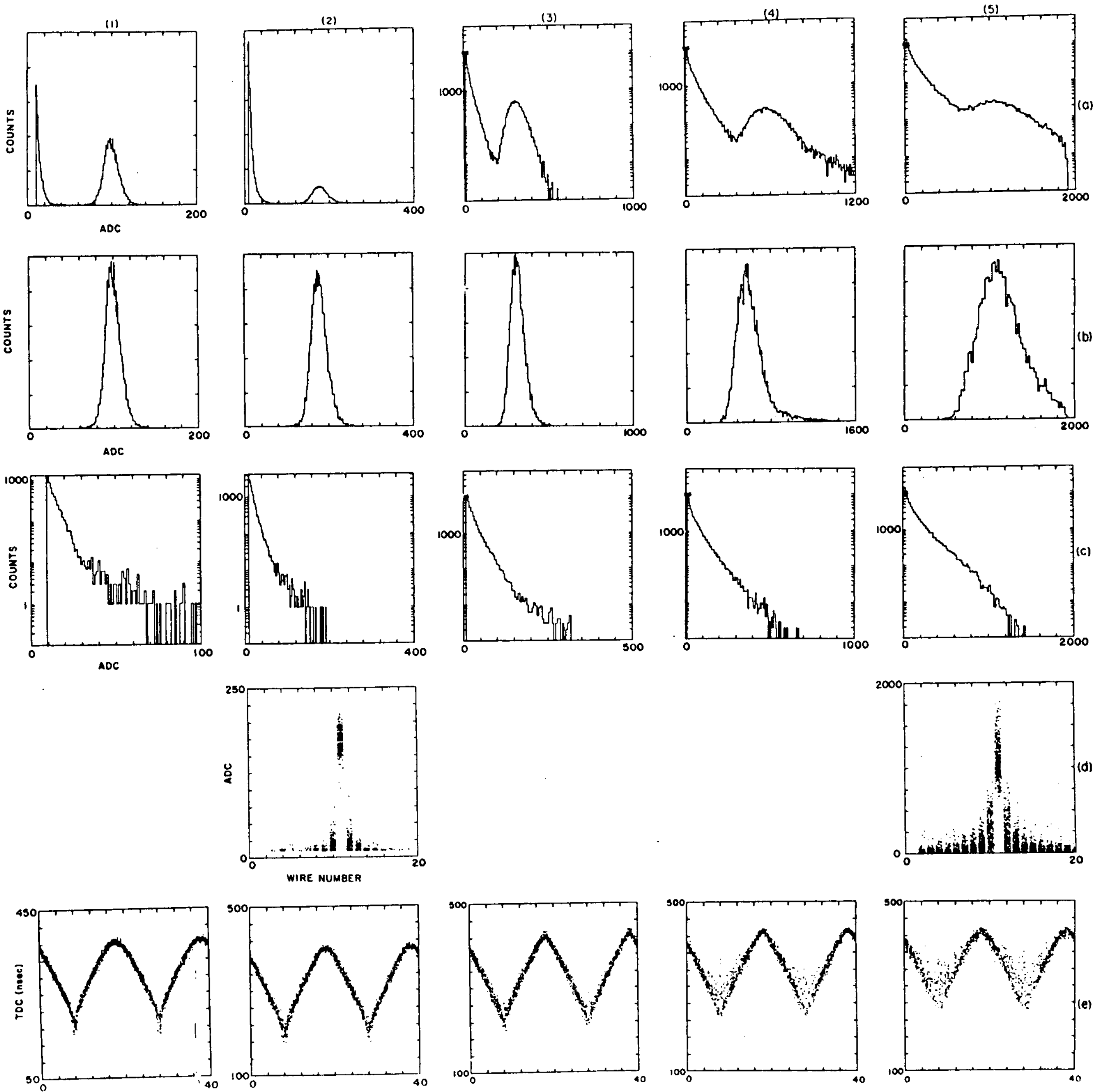
(1)
(2)
(3)
(4)
(5)
(a)
(b)
(c)
(d)
(e)
COUNTS
ADC
0
200
400
1000
1200
1600
2000
100
500
250
20
WIRE NUMBER
TDC (nsec)
450
50
100
40
X (mm)

Fig. 5-8

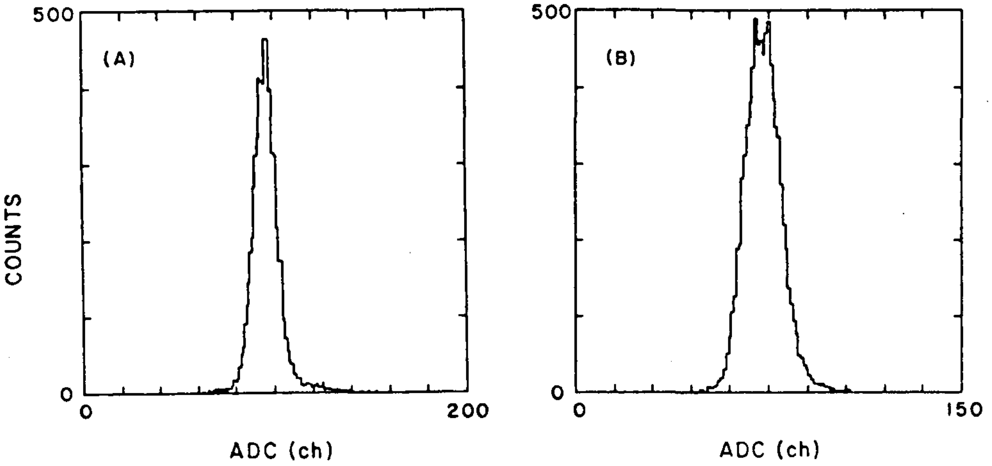

XBL 869-3303

Fig. 5-9

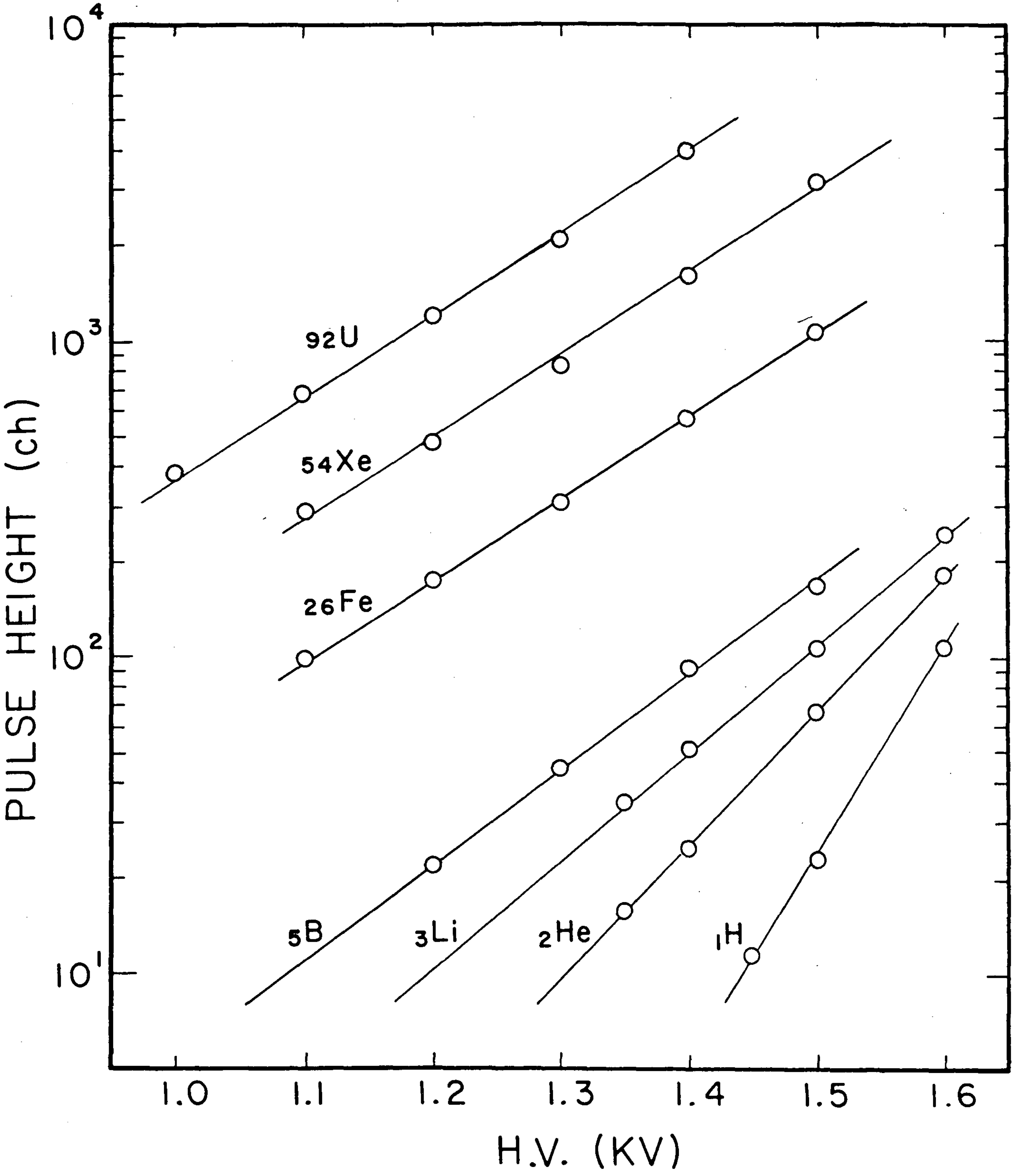

XBL 869-3308

Fig. 5-10(a)

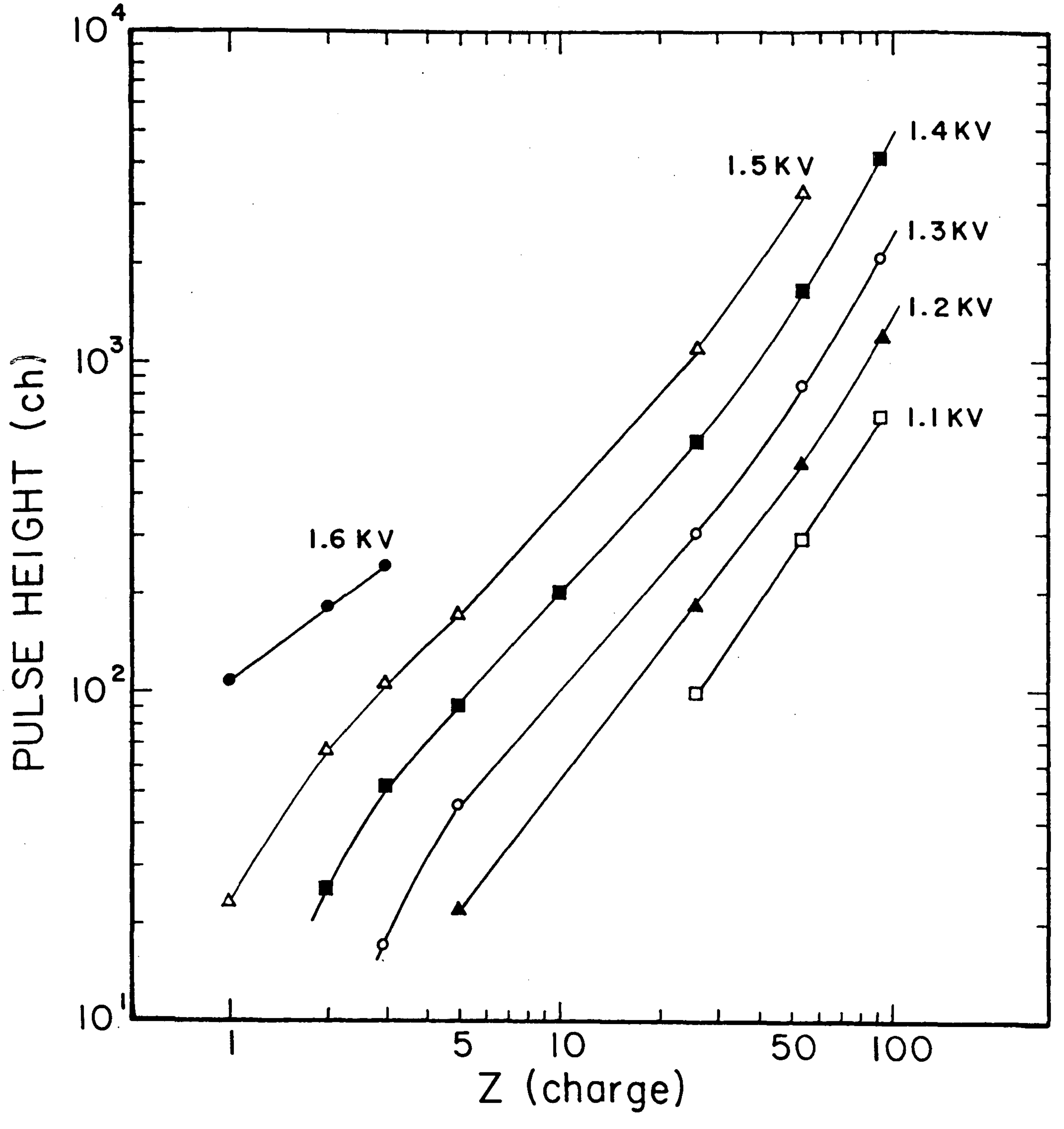

XBL 869-3315

Fig. 5-10(b)

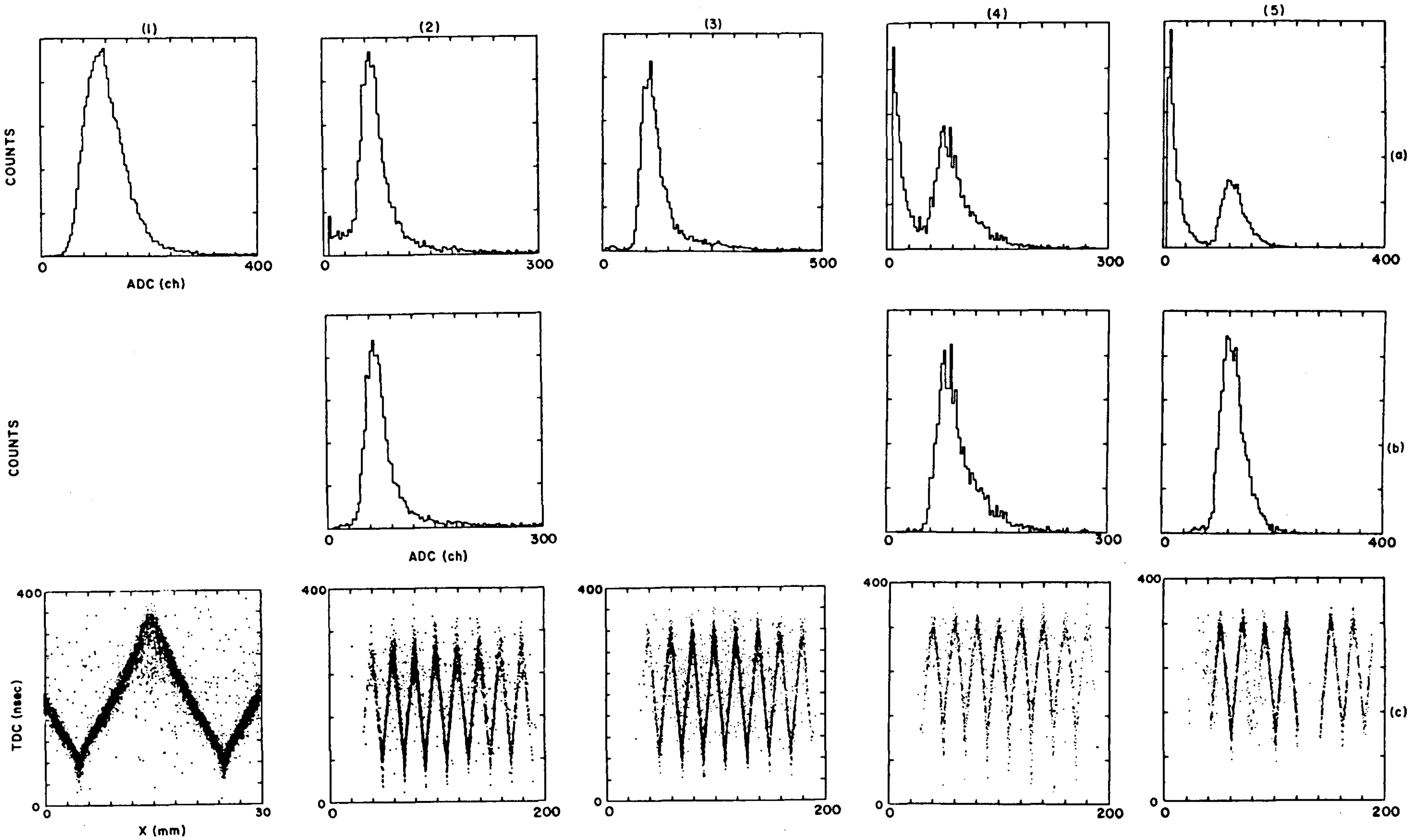

Fig. 5-11

XBL 869- 3320

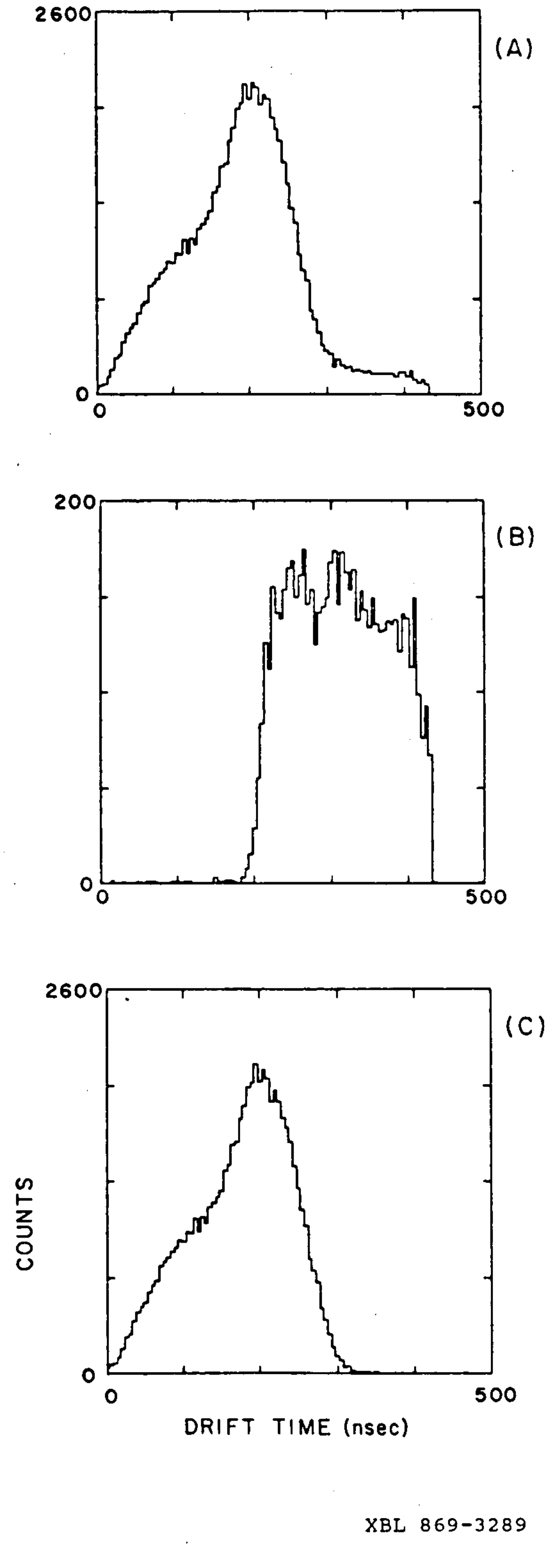

XBL 869-3289

Fig. 5-12

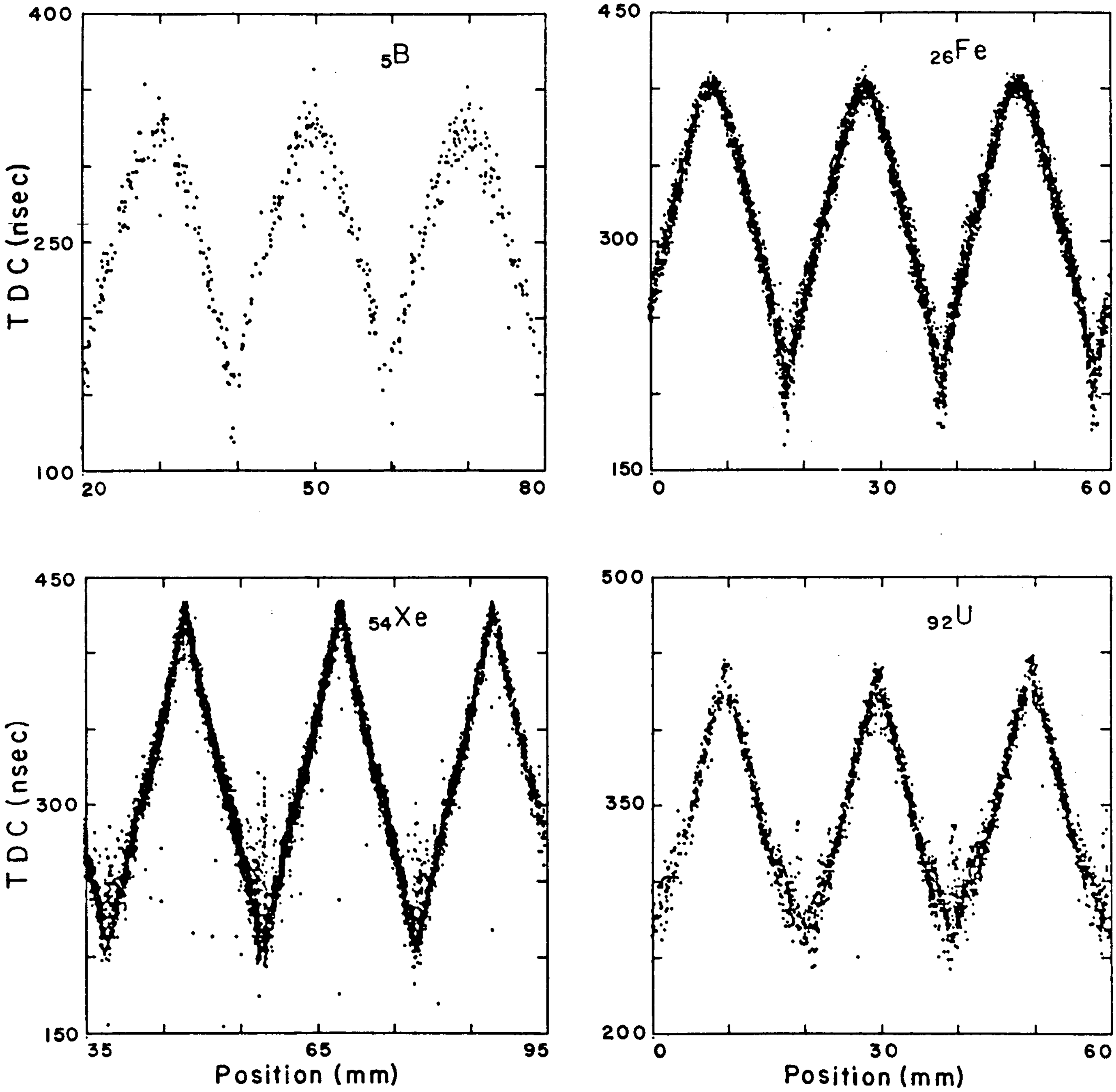

XBL 869- 3319

Fig. 5-13

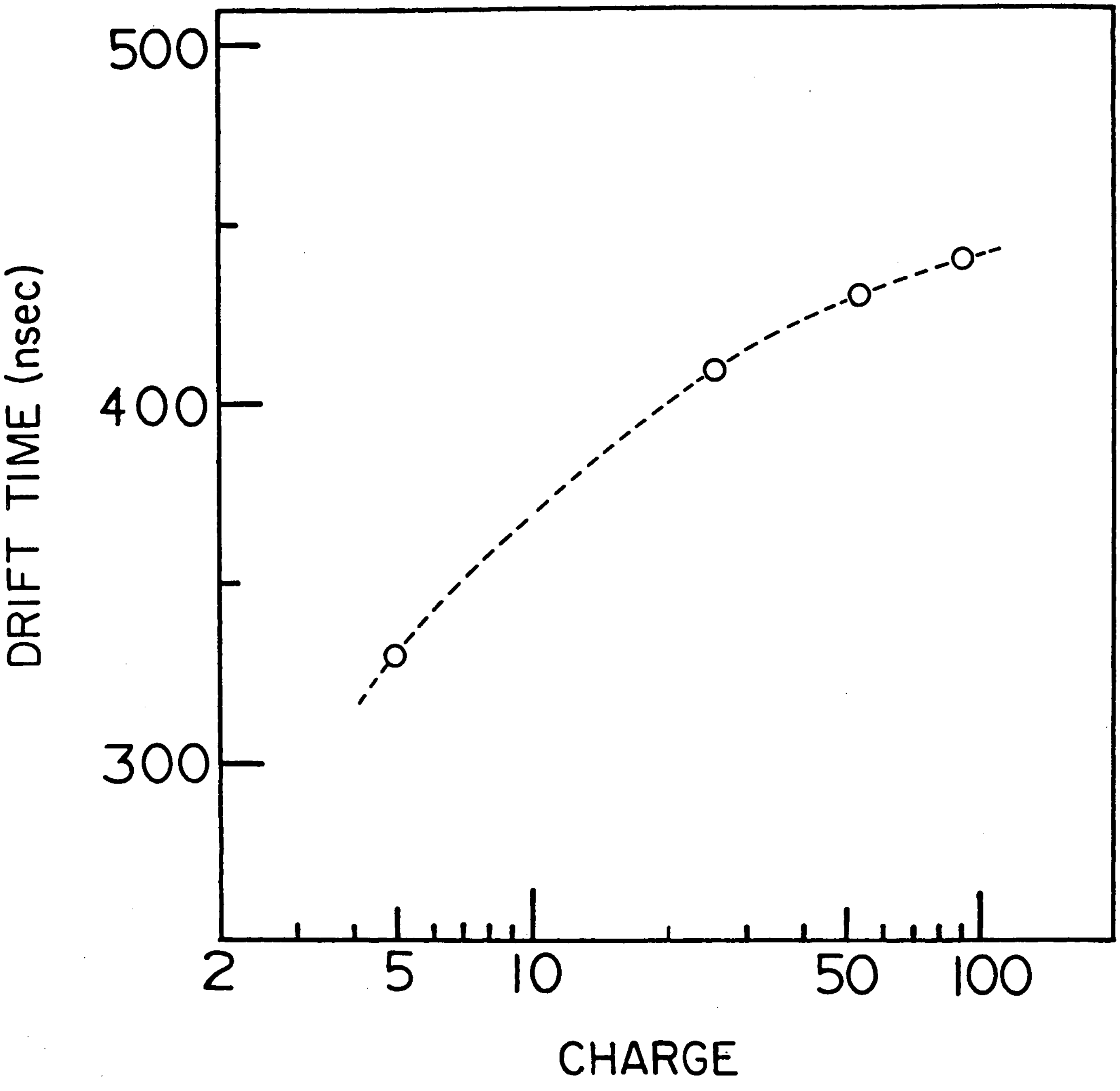

XBL 869-3306

Fig. 5-14

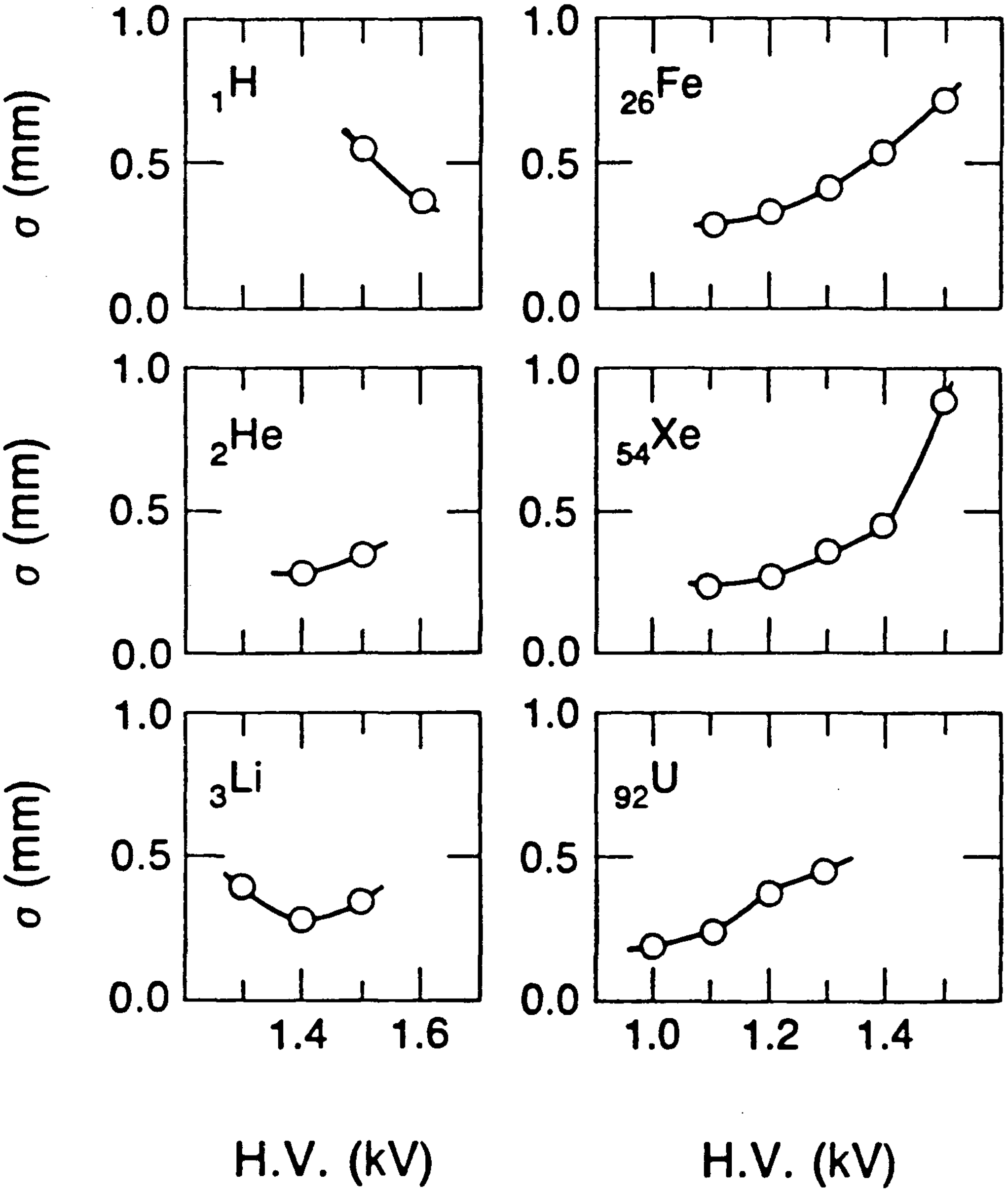

XBL 869-3294

Fig. 5-15

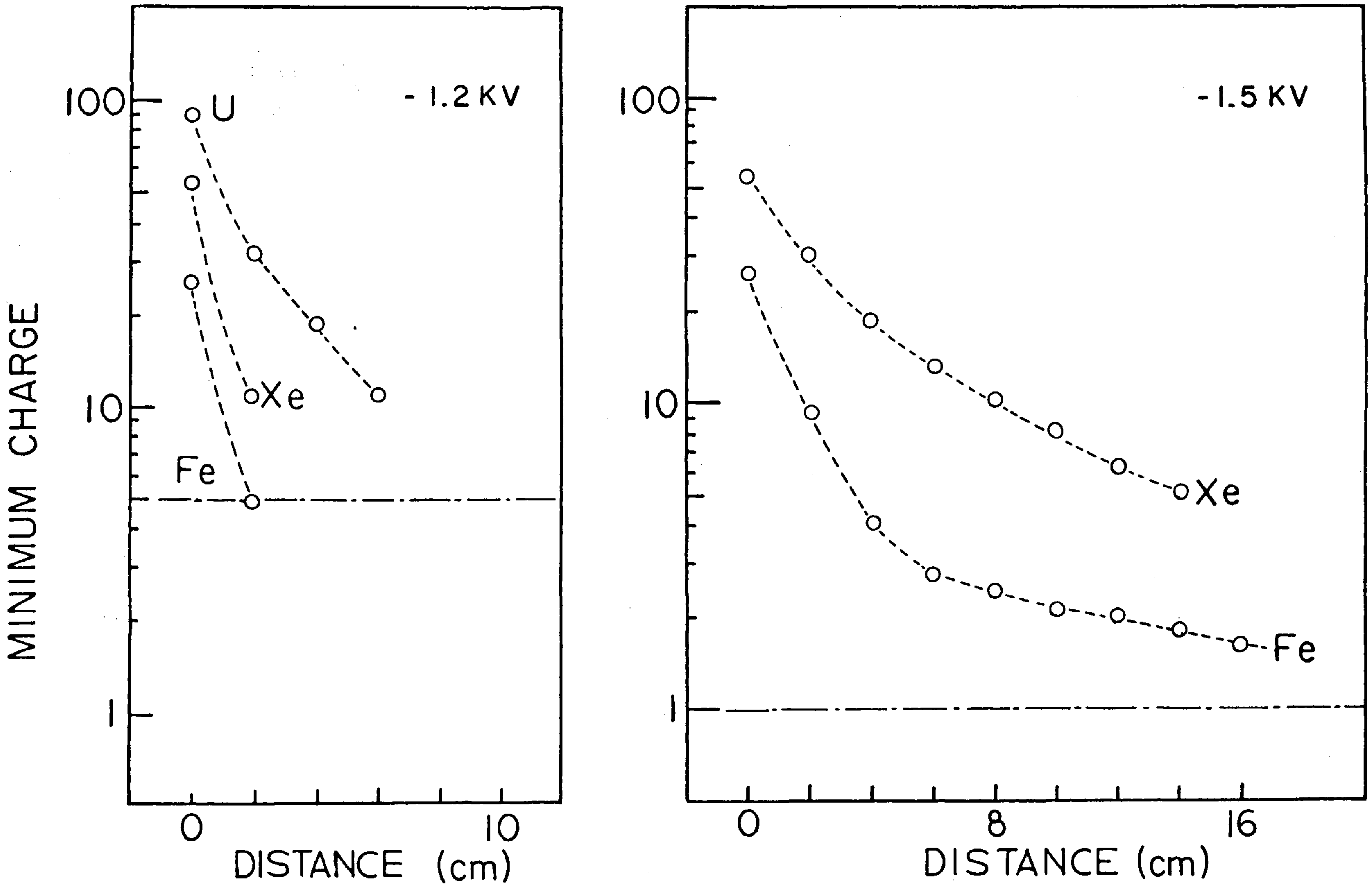

XBL 869- 3317

Fig. 5-16

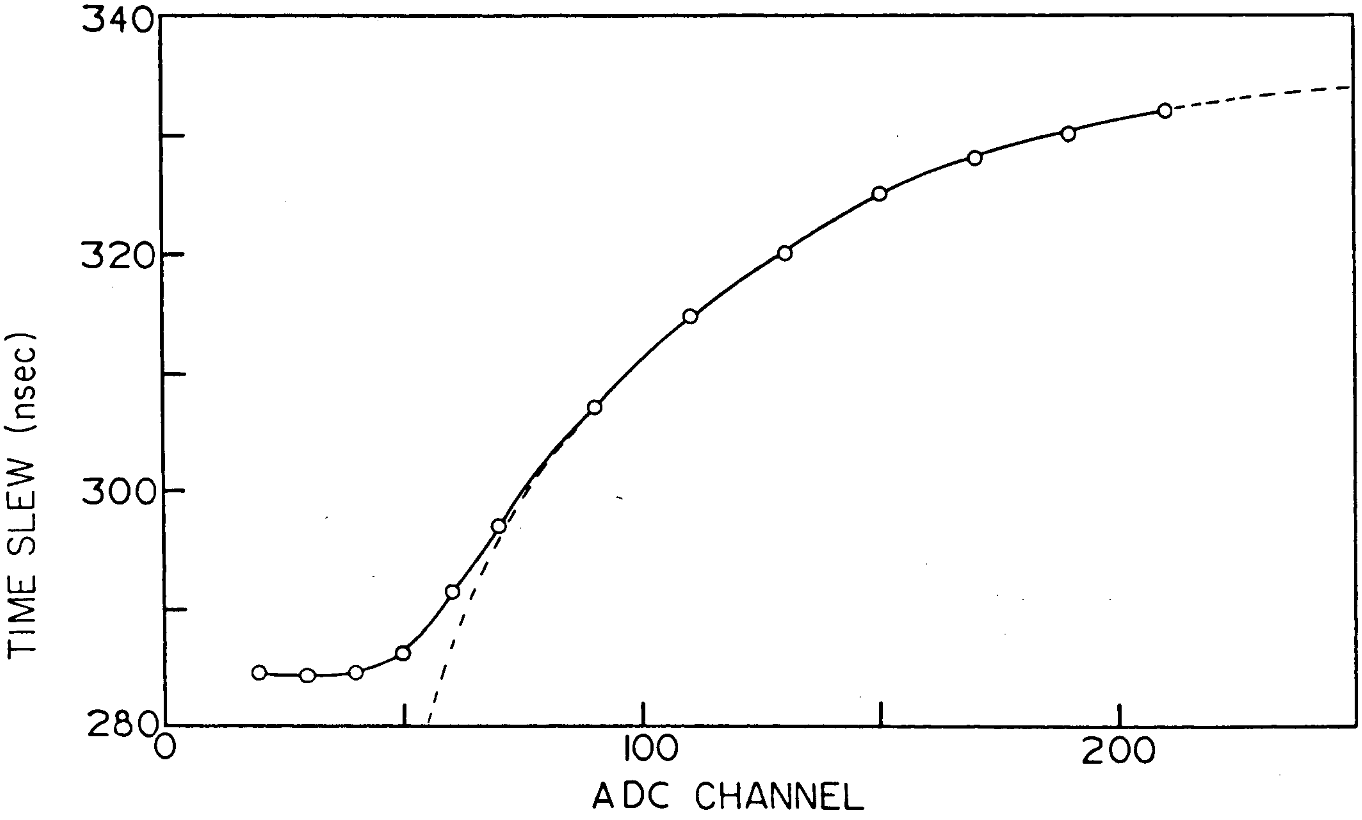

XBL 869-3307

Fig. 6-1

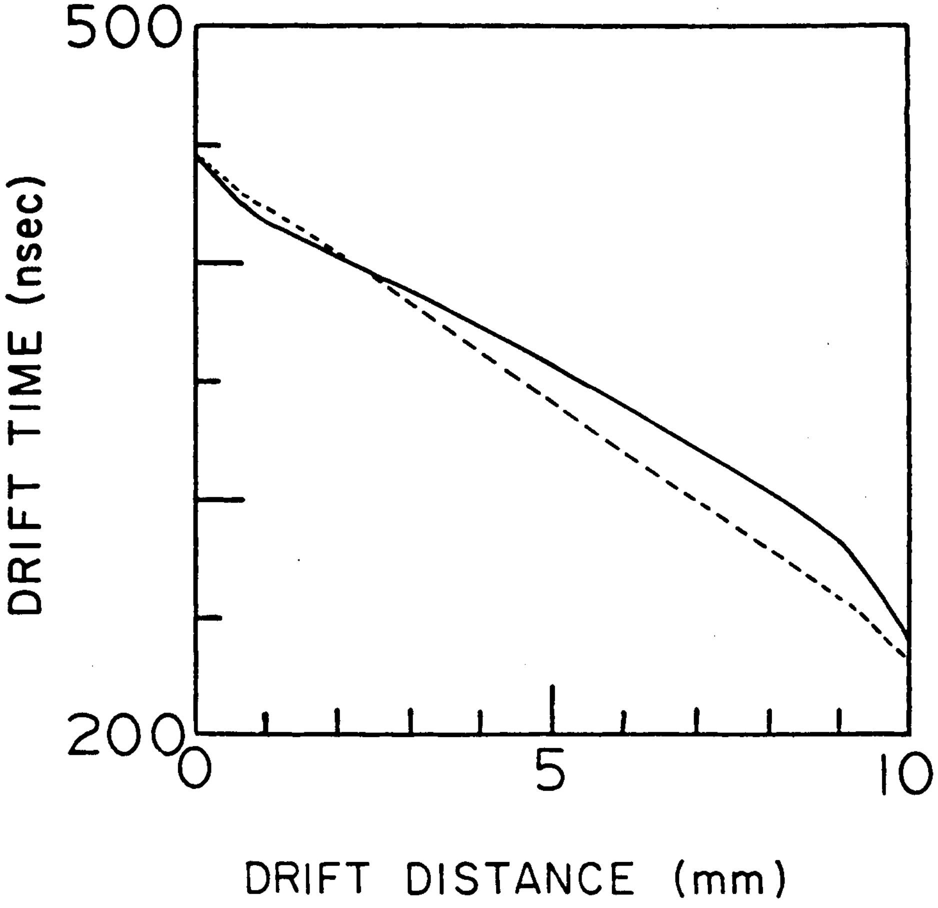

XBL 869-3296

Fig. 6-2

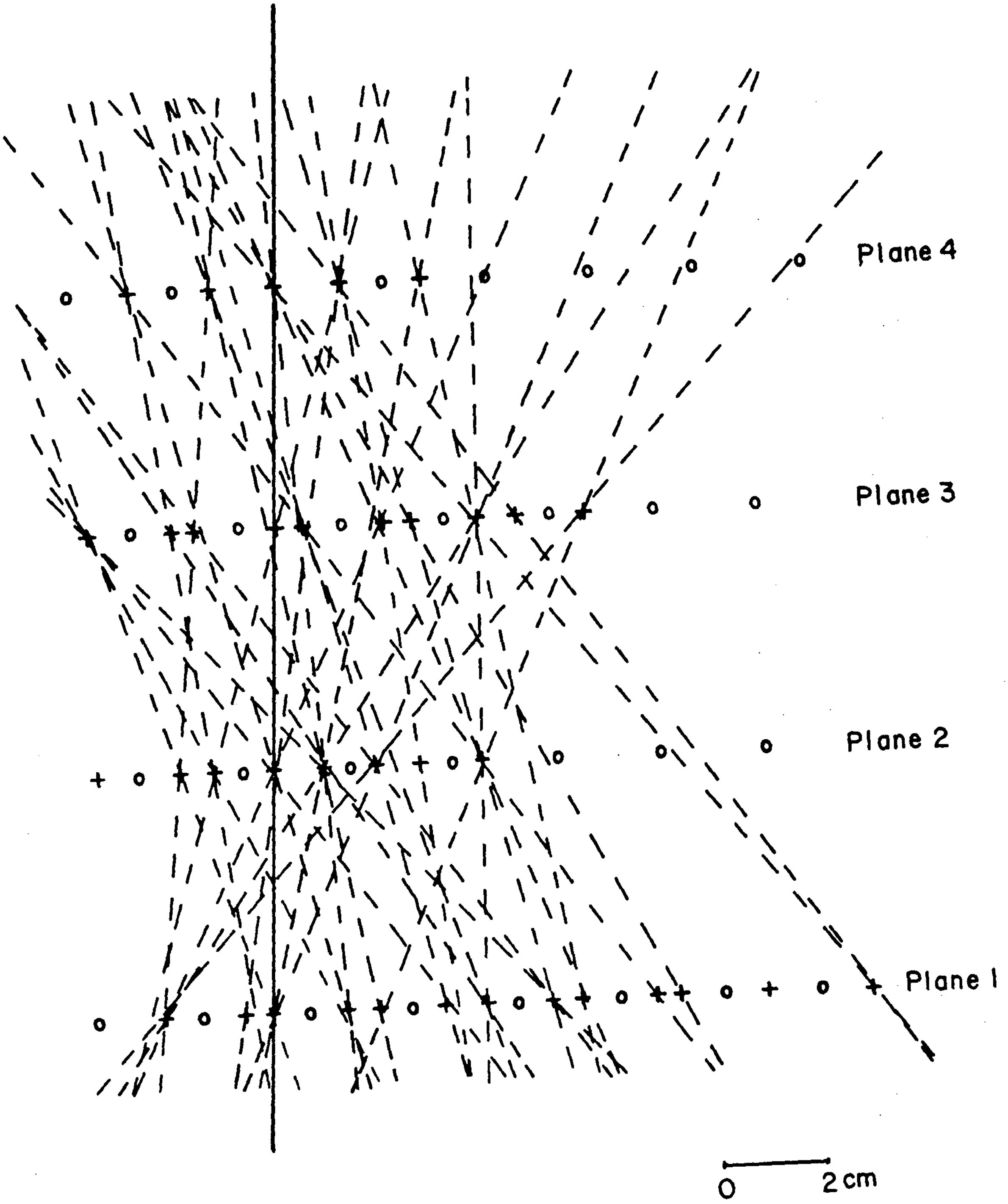

XBL 869-3302

Fig. 6-3

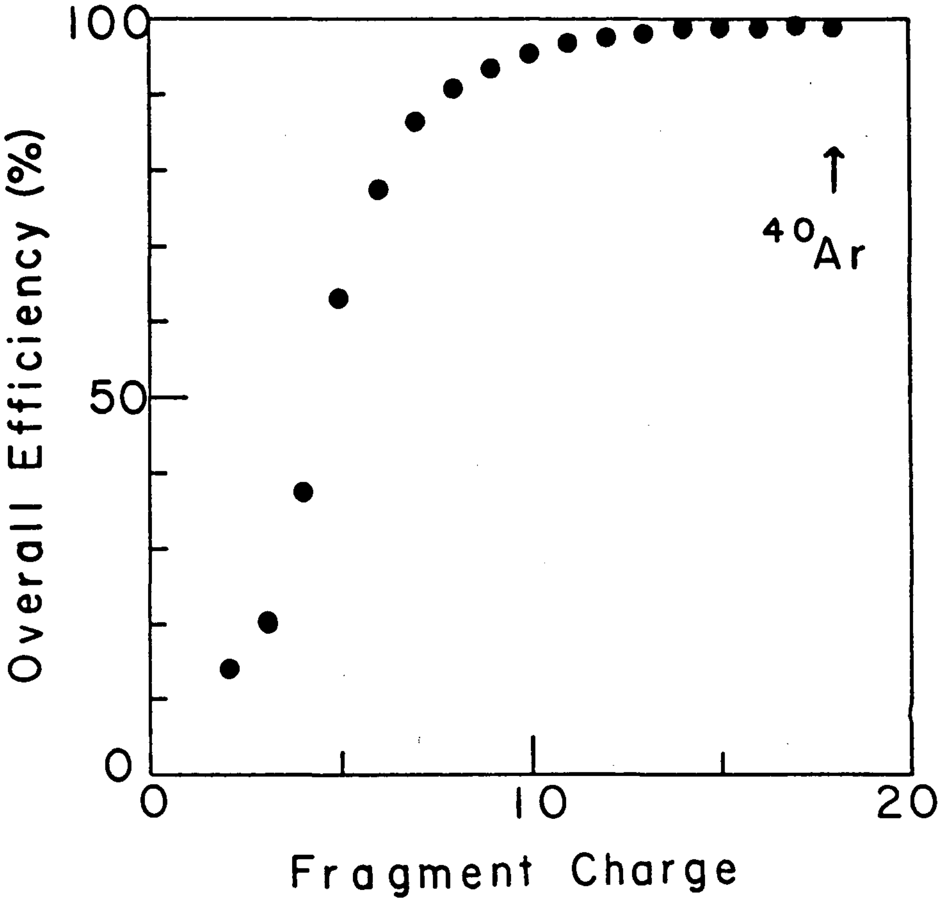

XBL 869-3299

Fig. 6-4

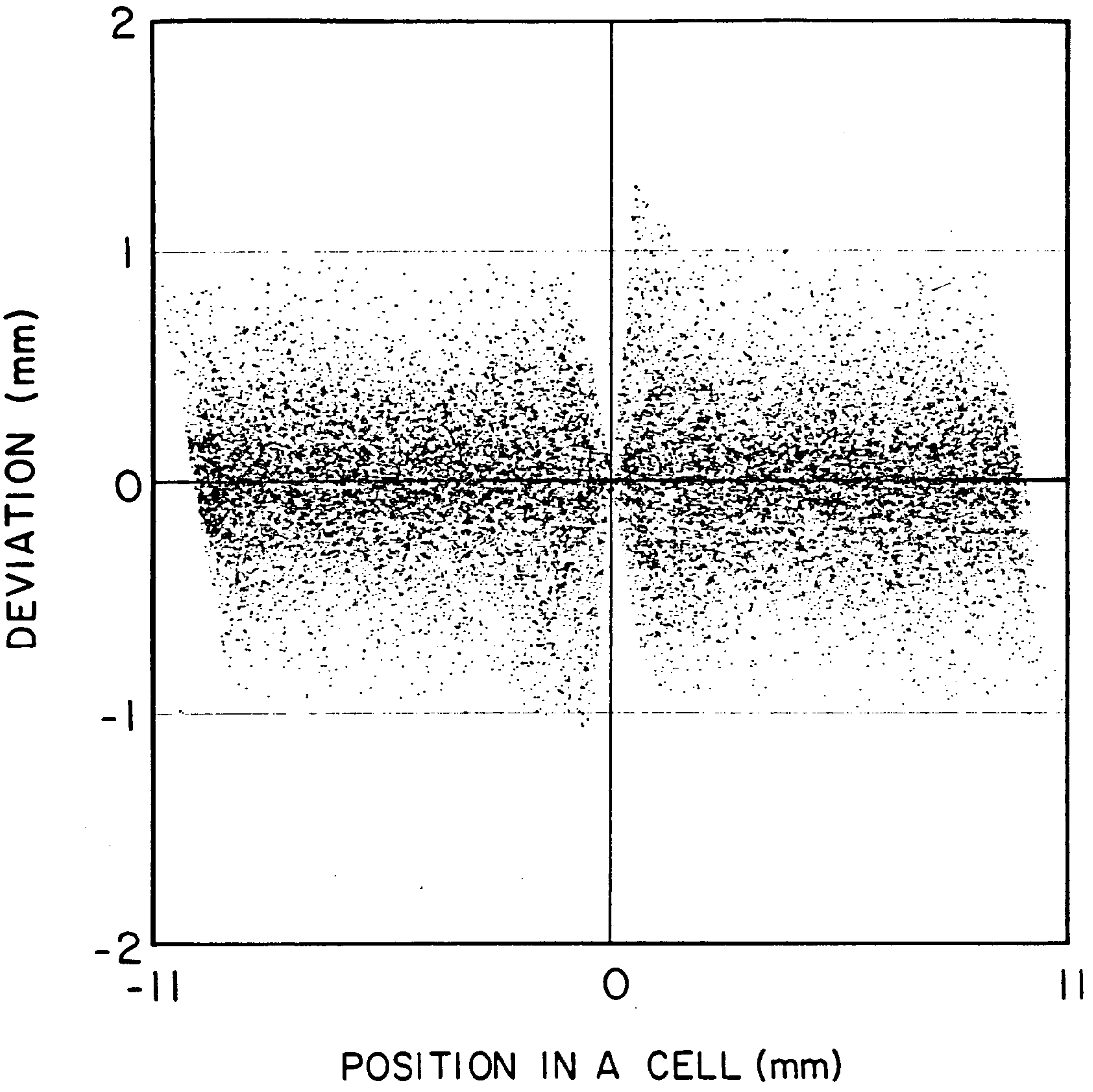

XBL 869-3300

Fig. 6-5

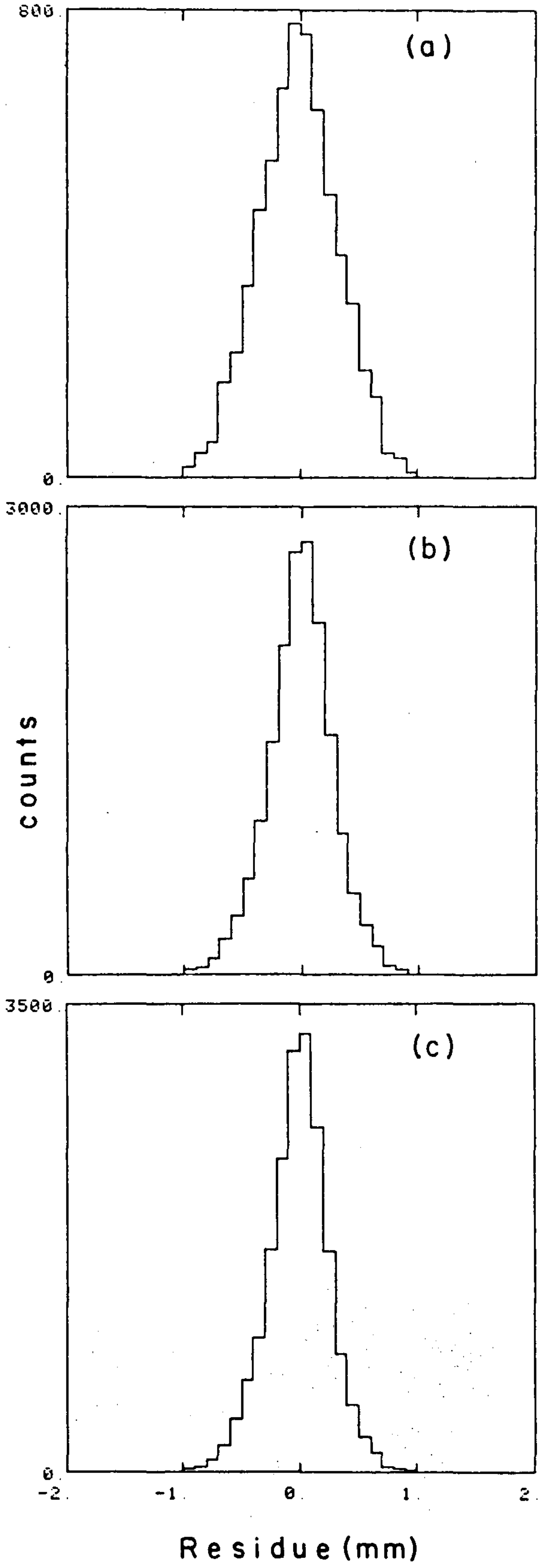

XBL 869-3305

Fig. 6-6

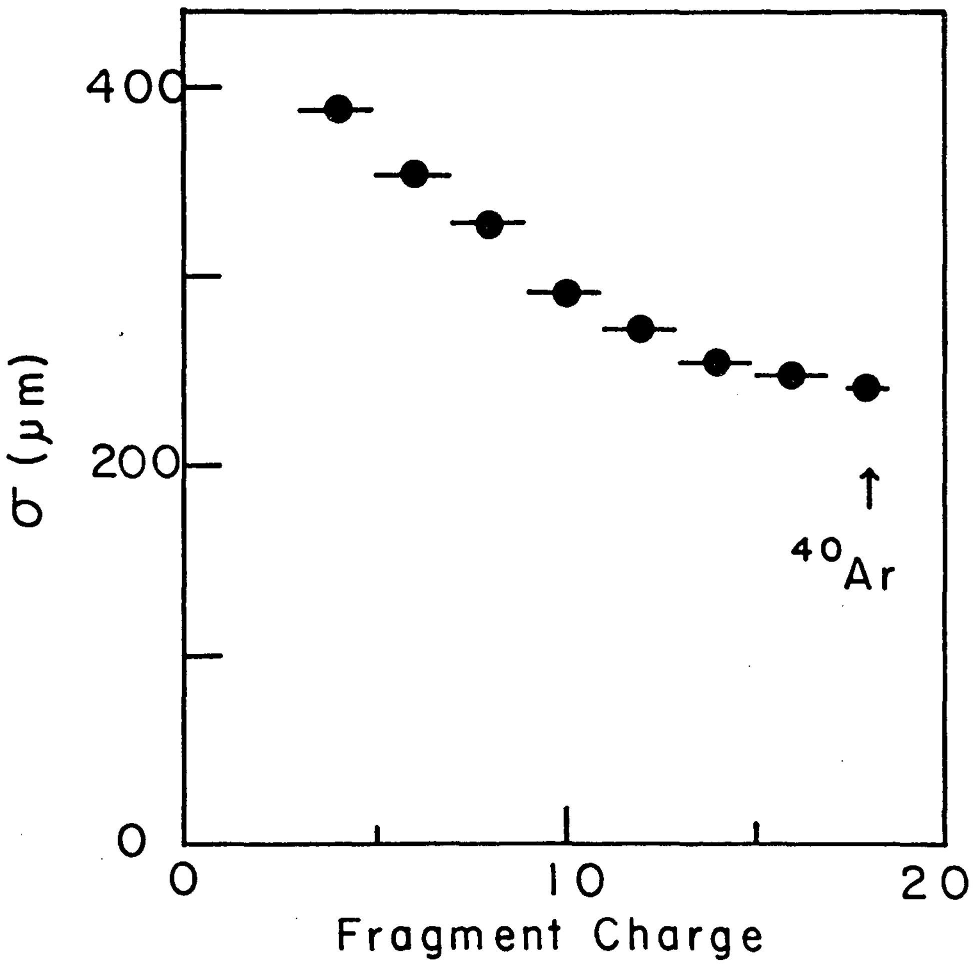

XBL 869-3298

Fig. 6-7

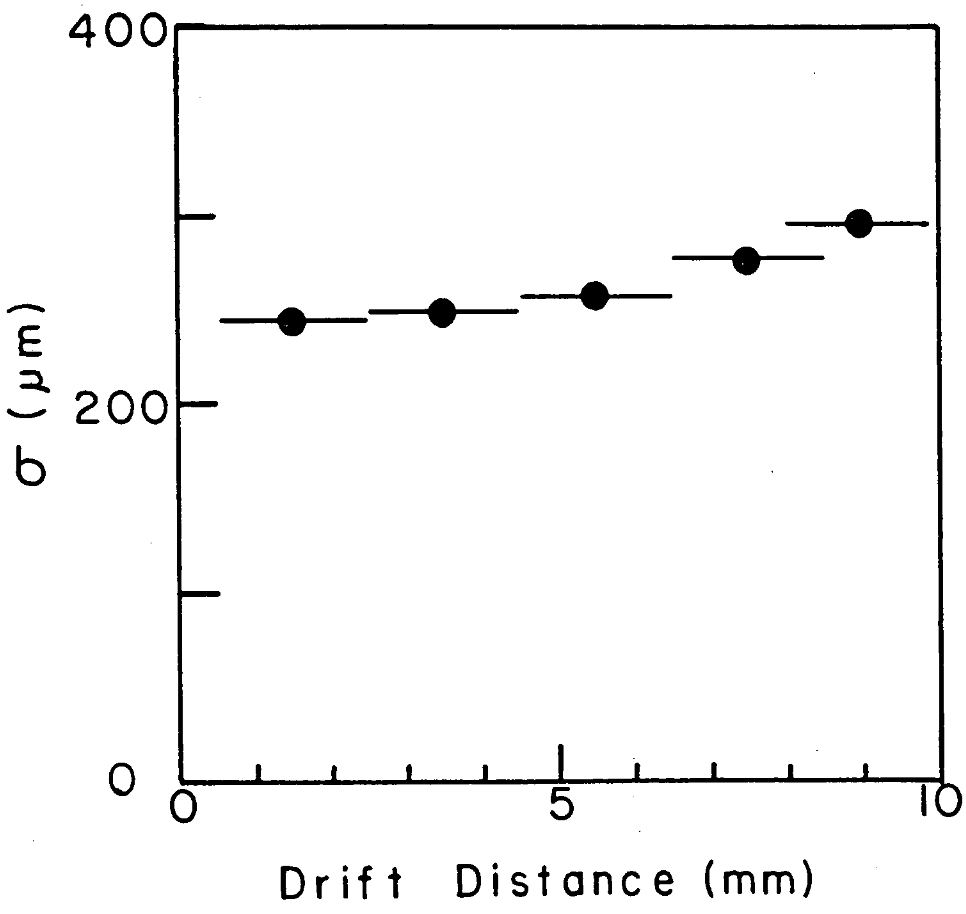

XBL 869-3297

Fig. 6-8

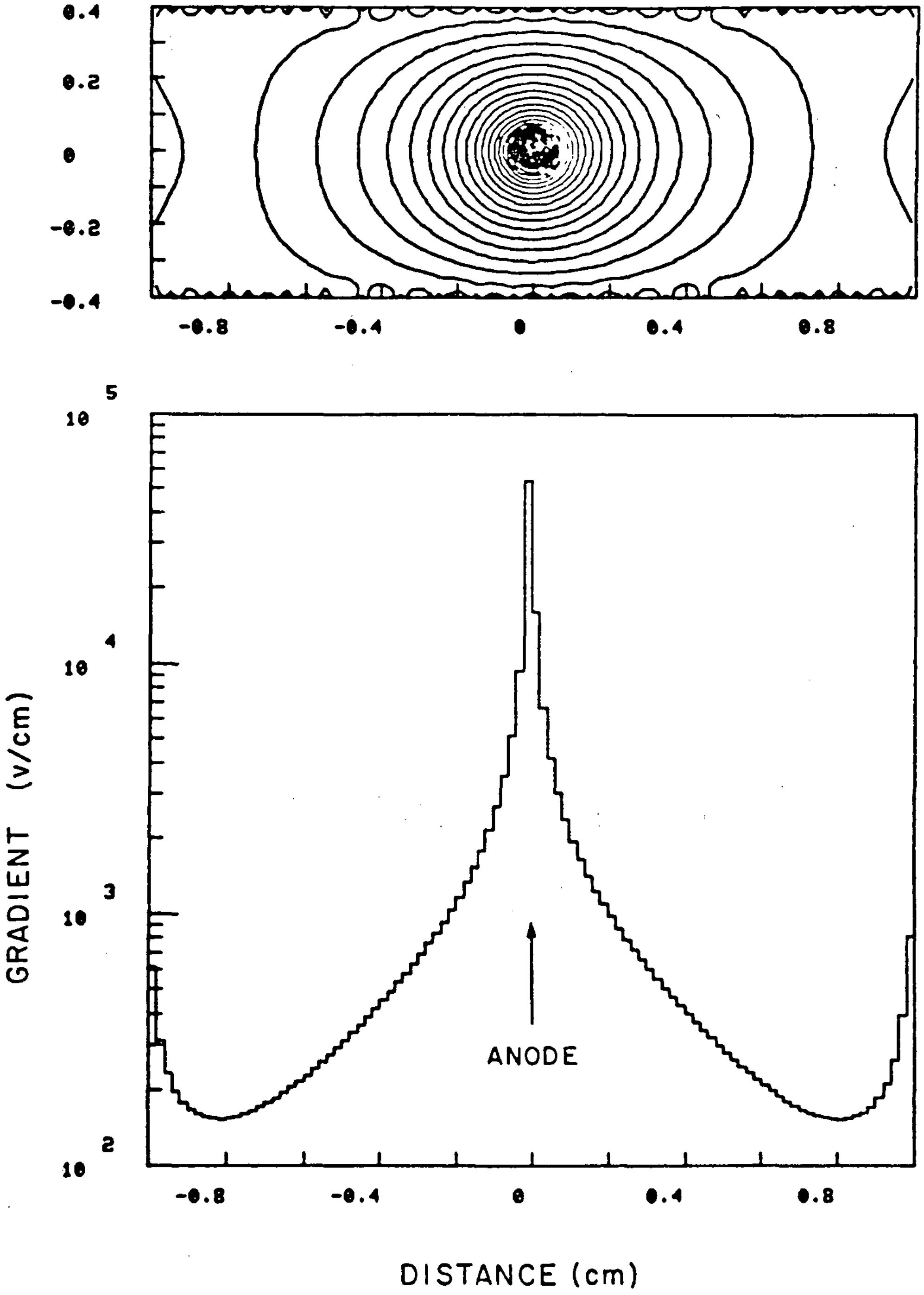

XBL 869-3288

Fig. 10-1

LAWRENCE BERKELEY LABORATORY
TECHNICAL INFORMATION DEPARTMENT
UNIVERSITY OF CALIFORNIA
BERKELEY, CALIFORNIA 94720